# Model development and numerical analysis of a vertical falling film absorption heat pump

Zhangxiang Wu [a, b], Shijun You [a, b], Tingting Jiang [a, b], Huan Zhang [a, b], Yaran Wang [a, b,*], Yan Jiang [a, b], Li Sha [a], Shen Wei [c]

[a] School of Environmental Science and Engineering, Tianjin University, Tianjin,300350, PR China

[b] Key Laboratory of Efficient Utilization of Low and Medium Grade Energy (Tianjin University), Ministry of Education of China, Tianjin 300350, PR China

[c] The Bartlett School of Construction and Project Management, University College London (UCL), 1-19 Torrington Place, London WC1E 7HB, United Kingdom

**ABSTRACT:** Traditional gas fired boilers and air-source heat pumps are not efficient for heating when the outdoor temperature is low, while the air-source heat pump is still one of the most promoting measures for building energy-efficient heating. In this study, a novel air-source gas-fired absorption heat pump with vertical falling film exchangers has been proposed for district heating. Compared with conventional gas fired boilers, the proposed system has higher efficiency, since it can absorb heat from the ambient air. A lumped and distributed parameter coupled numerical model is established to analyze its thermodynamic performance, together with a test rig established to validate the numerical model. Experimental results indicated that when the evaporator temperature increased from -10 ℃ to -5 ℃, the coefficient of performance rose from 1.53 to 1.62, and heating capacity improved from 36.88 kW to 45.32 kW. Additionally, the coupled model showed high prediction accuracy, with the maximum error less than 8%. Due to the opposite contributions of the supply water temperature and water flow rate to the coefficient of performance, the genetic algorithm was adopted to identify the optimal solution of

a multi-objective optimization procedure. Results displayed that the proposed system was feasible and efficient for heating in cold region under different operating conditions.

**KEYWORDS**: numerical analysis; coupled model; falling film heat transfer; absorption heat pump

| **Nomenclature** | | **Subscript** | |
|---|---|---|---|
| $c_p$ | constant pressure specific heat (J/kg·K) | abs | absorber |
| $COP$ | coefficient of performance | cond | condenser |
| $Cl_i$ | proximity index | evap | evaporator |
| EEV | electronic expansion valve | env | environment |
| $\Delta H_m$ | the heat of mixing of the R22-DEGDME (J/mol) | gen | generator |
| $h$ | specific enthalpy (J/kg) | he | heat exchanger |
| $H$ | molar enthalpy (J/kg) | in | inlet |
| $J$ | heat equivalent of work (g·m/J) | intf | interface |
| M | molecular weight (g/mol) | ng | natural gas |
| $m$ | mass flow rate (g/s) | out | outlet |
| $P$ | pressure (MPa) | r | refrigerant |
| $Q$ | heat transfer rate (kW) | s | strong |
| $T$ | temperature (K) | w | weak/water |
| $t$ | temperature (°C) | **Greek symbols** | |
| u | velocity in the x direction (m/s) | $\eta_b$ | boiler efficiency (%) |

| | | | |
|---|---|---|---|
| v | velocity in the y direction (m/s) | $\mu$ | Dynamic viscosity (kg/m·s) |
| $W_P$ | power input (kW) | $\xi$ | mass concentration (%) |
| $Y$ | molar concentration (%) | $\lambda$ | Thermal conductivity (W/m·K) |
| x,y | coordinate directions (m) | $\delta$ | film thickness (m) |

## 1. Introduction

With the growth of the thermal comfort requirements and improvements of human living standard, there has been a significant increase in building energy consumption, accounting for 20.6% of China's total energy consumption (Liu et al., 2020). While in northern China, the proportion of energy consumed by the district heating system in energy consumption of building sector is approximately 40%, mainly relying on fossil fuel (Zhang et al., 2020). Burning these fuels, however, will cause serious environmental issues, such as global warming and air pollution (Wu et al., 2019). Decreasing the energy demand of buildings is one of the greatest challenges for our society. However, according to the International Energy Agency (IEA), building energy consumption rose by 39% from 2000 to 2018, and it is expected to increase by more than 25% by 2040 (IEA., 2018). Therefore, the development of clean energy technologies and efficient heating solutions becomes necessary (Khalid R., 2019). As air is rich, clean and easy to access, many researchers have been investigating in developing air-source solutions for district heating (Wei et al., 2020).

In practice, the most efficient way of using the energy within the ambient air for

space heating is the heat pump technique, which can be categorized into two main types: the air-source absorption heat pump (ASAHP) and the air-source compression heat pump (ASCHP). The ASCHP systems have been widely studied by researchers. The coefficient of performance (COP) of the ASCHP systems can be higher than 3, although it highly relies on the ambient air temperature. Since the ASCHP is driven by electricity, the power generation efficiency should also be considered, when calculating the total COP from the primary energy (Lu et al., 2019). The ASAHP is superior over the conventional ASCHP in energy saving, environmental protection and low cost, since the total COP of the ASAHP from the primary energy is higher than that of the ASCHP (Wu et al., 2016). Anna et al. (2014) found that the absorption heat pump (AHP) has a lower impact on the environment than that of the compression heat pump (CHP). Zhang et al. (2014) compared an AHP system and a CHP system under the uniform heating quantity condition. They indicated that the district heating systems driven by AHP have lower energy consumption. With the same heating capacity and heating conditions, the primary energy efficiency (PEE) of the district heating systems driven by AHP can be higher for approximately 42% than those driven by CHP.

Although AHP systems are efficient methods for district heating, there are still limitations when using it at low ambient temperature in cold regions. Garimella et al. (1996) indicated that the COP of the generator-absorber heat exchange systems will rise from 1.05 to 1.4, when the ambient temperature increases from -30 ℃ to 5.6 ℃. Additionally, there are also some problems in choosing the working fluid. As the

72 water-lithium bromide working fluid will freeze at evaporation temperature below
73 0 ℃, while the ammonia-water working fluid is toxic and flammable. The two main
74 approaches for tackling these problems are designing novel systems and seeking for
75 new working fluids.

76 For designing novel systems, there have been numerous researches focused on
77 absorption-compression hybrid heat pump systems, which are superior in working at
78 low evaporation pressure and high absorption pressure (Wu et al., 2016). Wu et al.
79 (2018) investigated a compression-assisted AHP to extend the applicable conditions
80 and improve the heating performance. Results showed that the primary energy
81 efficiency of the compression-assisted AHP can be improved by 0.2-54% compared
82 with the conventional AHP. They also compared the thermodynamic performance of
83 AHP and compression-assisted AHP with different low-GWP working fluids. They
84 indicated that the compression-assisted AHP can improve the absorption pressure
85 and strengthen absorption process, leading to higher concentration difference (Wu et
86 al., 2017). This form of system improves the system performance by adding a
87 compressor, which in turn increases its complexity and initial cost. Another
88 improvement measure is to recover the excess heat of the flue gas (Lu et al., 2020).
89 There is considerable amount of waste heat contained within the high temperature
90 flue gas (Shang et al., 2017). Hence, recovering the flue gas waste heat is an efficient
91 way to improve the system energy efficiency (Khalid R., 2019). But in many cases,
92 the recovered waste heat is utilized by heating the return water of the district heating
93 system, and sometimes the return temperature is higher than the dew point of the

94 flue gas, which will lead to inefficient utilization of the excess heat from the flue gas
95 (Yang et al., 2018). Qu et al. (2014) designed a gas-liquid heat exchanger for the
96 AHP system. Both latent heat and sensible heat of the flue gas are recovered by this
97 system. They concluded that the heat recovery efficiency can be increased by 10%.
98 In addition, falling film heat exchangers applied in the AHP system has high heat
99 transfer coefficient under low heat flux compared with the conventional heat
100 exchangers in the refrigeration and air conditioning application (Hu et al., 2019).

101 Falling film heat exchangers with less working fluid and smaller size have been
102 widely used in AHP systems to achieve higher efficiency and lower cost (Robabeh et
103 al., 2020). However, most existing literature mainly involves the numerical and
104 experimental investigation on the single heat exchange tube flow and heat transfer.
105 Bundles falling film heat exchange process is more dependent on heat exchange
106 tubes steam direction and arrangement which have more complex mechanism of heat
107 transfer compared with single tube falling film. Saeed et al. (2021) investigated the
108 phase change mass transfer of the falling thin film on the surface of a vertical tube
109 and a series of remarkable evaporative heat transfer correlations are collected. Hu et
110 al. (2019) conducted a falling film heat exchanger simulation model applied to a
111 water vapor heat pump system. The temperature distributions of both the heat
112 exchanger and working tubes were obtained by finite element method. Liu et al.
113 (2017) proposed a system with four main vertical falling film heat exchangers and
114 set up a testing rig to examine the system's performance. They concluded that when
115 the pressure increases from 190 kPa to 260 kPa, the bilateral falling film renders the

absorbers generate steam more easily. Cheng et al. (2020) studied the falling film heat transfer characteristics of vertical tubes based on a series of experiments, and developed a model to accurately predict the performance of falling film. Liu et al. (2021) established a falling film heat exchanger experiment rig to measure the outer circumferential distribution of local heat transfer coefficient. According to their experimental data, the local heat flux distribution on tube surfaces was obtained by numerical calculation.

The existing gaps of improving the performance of air-source AHP systems are summarized as follows: 1) studies on new working fluid are needed, which can operate with high efficiency under cold ambient conditions; 2) hybrid absorption-compression heat pump systems is a good solution but with high cost compared with single AHP systems; 3) studies on flue gas heat recovery utilization below dew point is rare; 4) studies on the heat exchanger process of falling films in tube bundles are not sufficient. Therefore, this study has presented a novel gas-fired absorption heat pump using air-source for district heating. The proposed system is driven by natural gas and the working fluid is chosen as the R22-DEGDME. The ASAHP system can operate at the evaporation temperature below -10 ℃ with higher COP. To reduce the flow rate and pump power, both the absorber and generator are considered as falling film heat exchangers, which have high heat transfer coefficients. A coupled lumped parameter and distributed parameter numerical model is developed to analyze the system performance, together with an experimental rig designed for model validation. In addition, a multi-objective optimization approach

is applied to optimize the system performance using the NSGA-II approach and TOPSIS decision-making method. This system provides a feasible and efficient method to collect more energy from ambient air for district heating, and it is technologically available in different heating capacities with the following contributions:

1) The system can sufficiently recover the flue gas waste heat and operate at low outdoor temperature with high efficiency.

2) A coupled model with satisfied prediction accuracy including distributed parameter numerical and lumped parameter model has been established.

3) The two-dimensional distributed parameter models of the generator and absorber in the ASAHP system are proposed and validated.

## 2. System description

### 2.1. Fundamental

A schematic diagram of the ASAHP systems is displayed in Fig. 1. The ASAHP consists of three circuits, the black line for working fluid circuit, the blue line for the hot water circuit, the green and purple lines for solution circuits. In the refrigerant loop, the refrigerant vapor generates from the generator enters the condenser to heat the supply water. The refrigerant vapor condenses into liquid and goes to the reservoir. In the exchanger-II, the refrigerant vapor from the evaporator is heated by the liquid refrigerant from the reservoir. Then the refrigerant condensing pressure decreases to the evaporation pressure in the EEV. The low pressure and temperature

refrigerant is heated by the ambient environment in the evaporator. Finally, the refrigerant vapor from the evaporator turns to the absorber.

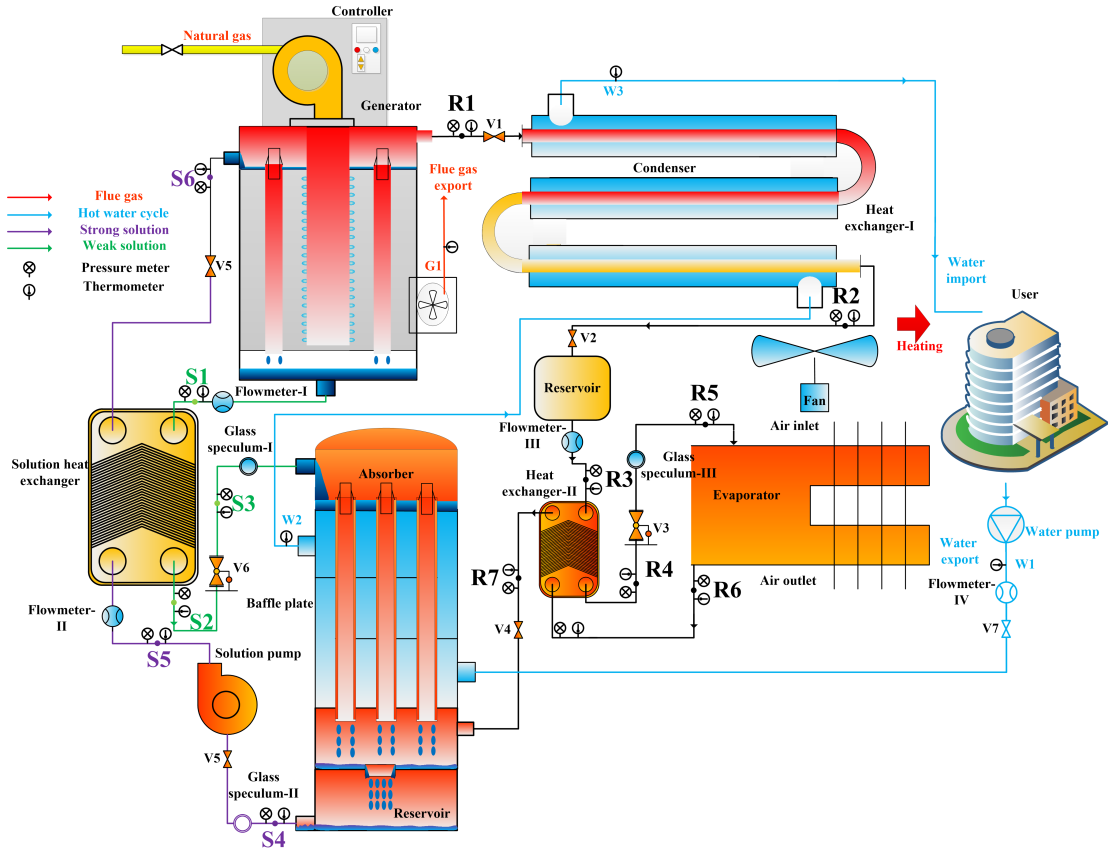


Fig. 1 Schematic view of a typical ASAHP system

There are three working fluids which are refrigerant, strong solution and weak solution. The strong solution contains more refrigerant with the refrigerant mass fraction of 30%; while the weak solution contains less refrigerant with the refrigerant mass fraction of about 18%. The whole circulation starts from the absorber. The refrigerant vapor from the evaporator is absorbed by the weak solution in the absorber, and becomes strong solution. The supply water is heated by the mixture of the refrigerant vapor and weak solution. In the solution heat exchanger, the strong solution extracted from the absorber exchange heat with the weak solution from the generator. Then the strong solution pumped by the solution pump enters the

generator. The strong solution absorbs heat from the combustion of natural gas and produces refrigerant vapor when the solution temperature reaches the refrigerant boiling temperature. Then the refrigerant concentration of the solution decreases and the strong solution becomes weak solution. The weak solution goes to the solution heat exchanger while the refrigerant vapor enters the condenser. The generator pressure reduces to the absorber pressure by the EEV throttling process and the weak solution is returned to the absorber. In the condenser and absorber, the return water from the user is heated to the set supply water temperature.

According to the existing theoretical analysis, a test rig has been developed for the ASAHP system, as shown in Fig. 2. All the valves and two EEVs controlled by independent controllers are opened before the startup of the system. Due to the limitation of experimental conditions, the flue gas waste heat was not recovered, but left for future investigations. The experimental system runs based on the following steps: 1) the combustion chamber is opened by the controller; 2) it turns on the fixed volume solution pump and started the circulation of the solution, and 3) it starts fan coils and water pumps to for water circulation.

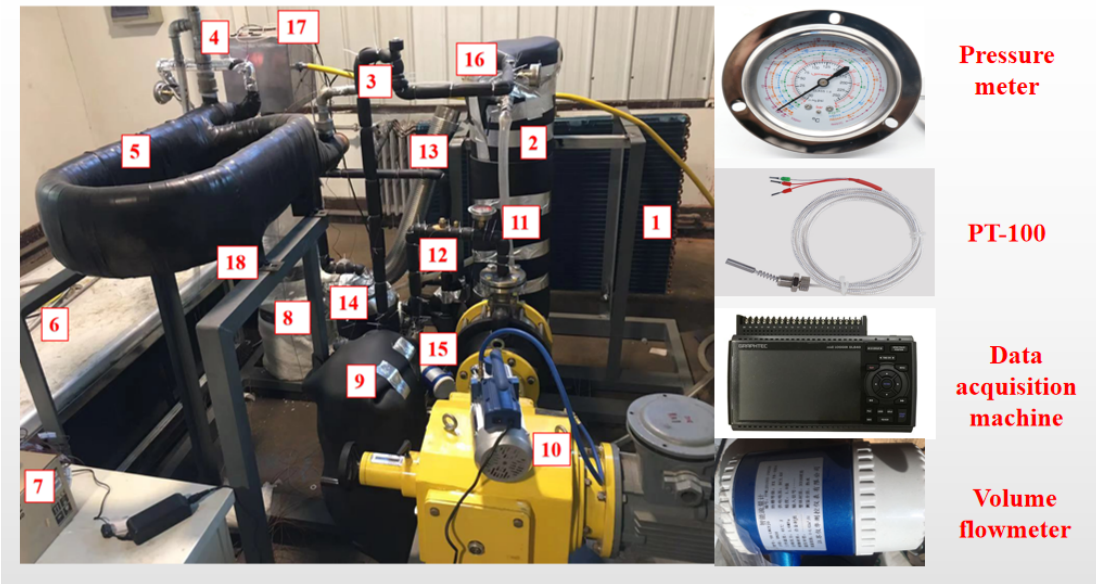


(a) Photo of the test bench

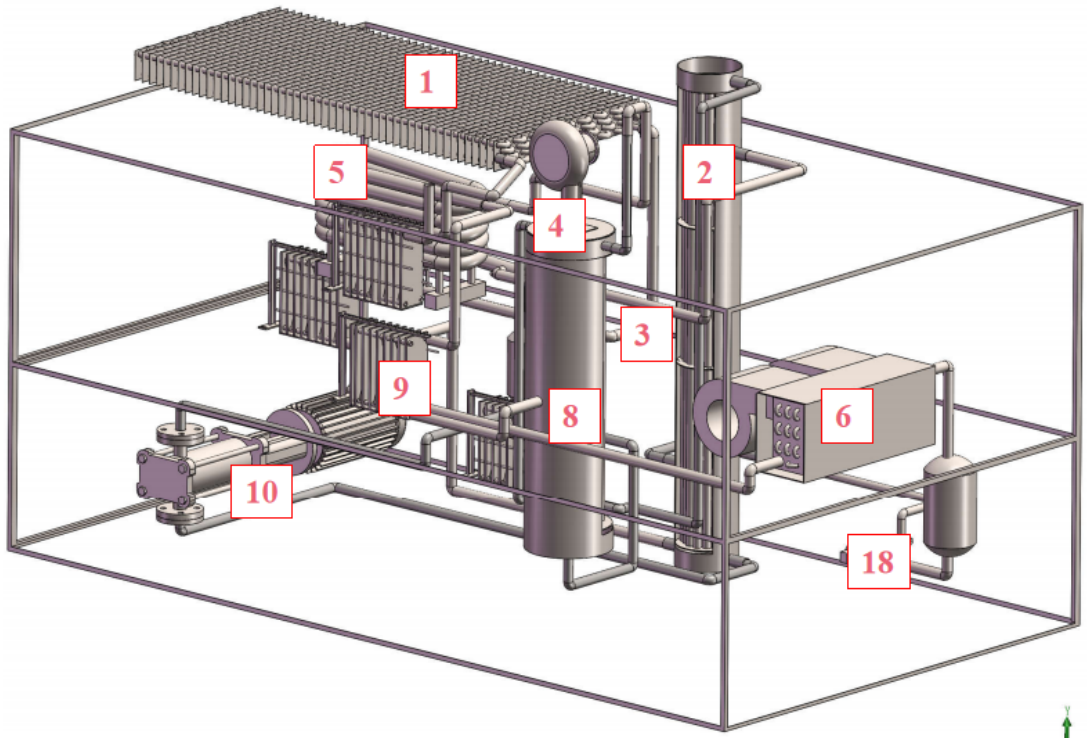


(b) 3-D geometric model of the test bench

1-Evaporation, 2-Absorber, 3-EEV, 4-Combustor, 5-Condenser, 6-Fan coil, 7-Data acquisition machine, 8-Generator, 9-Solution heat exchanger, 10-Solution pump, 11-Pressure meter, 12-Valve, 13-Chimney, 14-Reservoir, 15-Volume flowmeter, 16-Glass speculum, 17- Controller,

18-Water flowmeter

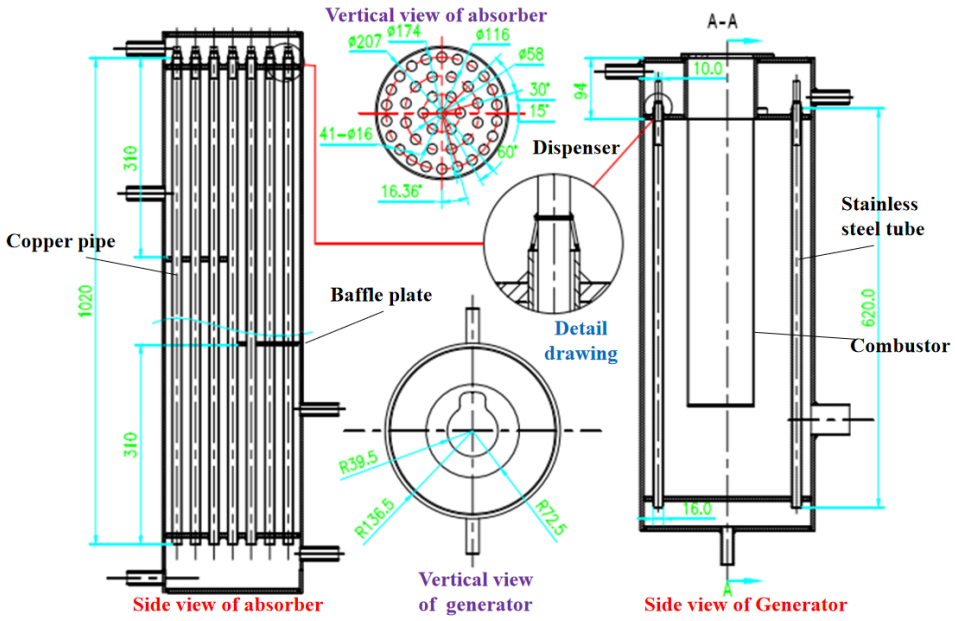


(c) Design drawings of absorber and generator

Fig.2 Test rig and design drawings of absorber and generator

Suitable selection of working fluids is significant which has the following advantages: 1) improving energy conversion efficiency; 2) reducing irreversible destruction. AHP systems with ammonia-water and water-lithium bromide pairs have been studied by many researchers. However, both working pairs have disadvantages. For example, a system with water-lithium bromide as the working fluid will not work at an evaporation temperature below 0 ℃ because water freezes, which cannot be used in cold regions (Nico et al., 2020). Ammonia, however, is flammable and toxic (Yuan et al., 2018). In the air-source gas-fired AHP, the system with ammonia-water as the working fluid has obvious hazards. Solution of R22-DEGDME is non-toxic and non-flammable, which can work below the outdoor temperature of 0 ℃ (Wu et al., 2020). This solution with high GWP and ODP,

however, cannot be extensively applied in the future (Ando et al., 1984). As system with R22-DEGDME working pair has better operating performance, this, however, indicates some different direction and operating guidance for system design and working pair selection. According to the Kigali Amendment, R22 with high GWP and ODP cannot be applied. In the Table A1, some properties of the solution are displayed.

## 2.2. Experimental components and operating conditions

Table 1 presents the main equipment of the proposed system, and Table 2 displays the detailed experimental design conditions.

Table 1 Equipment of the proposed system

| Equipment | Types | Specifications |
|---|---|---|
| Heat exchanger-II | PL26-20 | Heat load: 3 kW; heat exchanger area: 1.5 $m^2$. |
| Condenser | Double-pipe exchangers TH-SCE25 | Heat load: 25 kW ; heat exchanger area: 12 $m^2$. |
| Water pump | LRS-9 | Flow rate: 0 -7.8 $m^3/h$ |
| Generator | Vertical falling film | Heat load: 24 kW; heat exchanger area: 0.36 $m^2$. |
| Absorber | Vertical falling film | Heat load: 15 kW; heat exchanger area: 1.2 $m^2$. |
| Fan coil | BFP-70WD | Cooling capacity: 50 kW; air volume: 7000 $m^3/h$ |
| Evaporator | Finned tube exchanger DYGT-15 | Heat load: 15 kW; heat exchanger area: 28 $m^2$. |
| Flowmeter | YH-LWGYJD | Flow rate: 0-6.62 $m^3/h$ |
| Solution heat exchanger | PL95-86 | Heat load: 130 kW; heat exchanger area: 10 $m^2$. |
| EEV | PCH-SD1N-002 | - |
| Pressure meter | RL-2088 | - |
| Thermometer | PT-100 | Pressure: -0.1 to 60 MPa |
| Solution pump | Metering pump TL-D1800 | Flow rate: 1.74 $m^3/h$ |
| Data acquisition machine | GRAPHTEC-GL840 | - |

Table 2 System working conditions

| Variables | Range |
|---|---|
| Condensing temperature | 38 °C - 45 °C |

| | |
|---|---|
| Evaporating temperature | -10 °C - 0 °C |
| Generator temperature | 150 °C - 190 °C |
| Water flow rate | 1.5 m³/h - 2.4 m³/h |
| Volume of the solution pump | 70% - 100% |

## 2.3. Uncertainty analysis

In the system shown in Figs. 1 and 2, temperature, flow rate and pressure are obtained by the data acquisition instrument in the experiment for further analysis. Therefore, uncertainty analysis becomes necessary to evaluate the experimental data. The total uncertainty is divided into random uncertainty and system uncertainty, as defined by Equation 1 (Lu et al., 2020),

$$\sigma_T = \sigma_R + \sigma_s \tag{1}$$

According to the uncertainty analysis theory, if there are $n$ measured variables, the related directly-measured parameters are applied to calculate the total uncertainty (Lu et al., 2020). If $y$ is a function of $x_1$, $x_2$, ..., $x_n$, as defined by Equation 2,

$$y = f(x_1, x_2, ..., x_n) \tag{2}$$

The function y total uncertainty can be calculated by Equation 3 (Lu et al., 2020),

$$\sigma_T = \sqrt{\left(\frac{\partial f}{\partial x_1}\sigma_{T,x_1}\right)^2 + \left(\frac{\partial f}{\partial x_2}\sigma_{T,x_2}\right)^2 + \cdots + \left(\frac{\partial f}{\partial x_n}\sigma_{T,x_n}\right)^2} \tag{3}$$

Taking the heat load as an example, the total uncertainty could be written as follows (Lu et al., 2020),

$$Q = c_{p.w}\rho V(T_1 - T_2) \tag{4}$$

$$\begin{aligned}\sigma_T &= \sqrt{\left(\frac{\partial f}{\partial V}\sigma_{T,V}\right)^2 + \left(\frac{\partial f}{\partial T_1}\sigma_{T,T_1}\right)^2 + \left(\frac{\partial f}{\partial T_2}\sigma_{T,T_2}\right)^2} \\ &= c_{p.w}\rho\sqrt{(T_1 - T_2)^2\sigma_{T,V} + V^2(\sigma_{T,T_1}^2 + \sigma_{T,T_2}^2)}\end{aligned} \tag{5}$$

## 3. Numerical model

Fig.3 displays the P-T and T-S figure of different processes. To analyze the system performance, a coupled model including a lumped parameter model and a distributed parameter model have been established, with the following assumptions for simplification:

1) Both system components and thermodynamic processes are stable.
2) Constant pressure in the absorber and generator.
3) At the condenser and evaporator outlets, refrigerants are considered as saturated.
4) Ignoring the pressure drop and heat loss (Lu et al., 2019).
5) The two-dimensional model for the heat and mass transfer process is employed for the falling film absorber and generator.
6) The liquid and vapor flows are considered to be steady, laminar, and Newtonian (Robabeh et al., 2018).

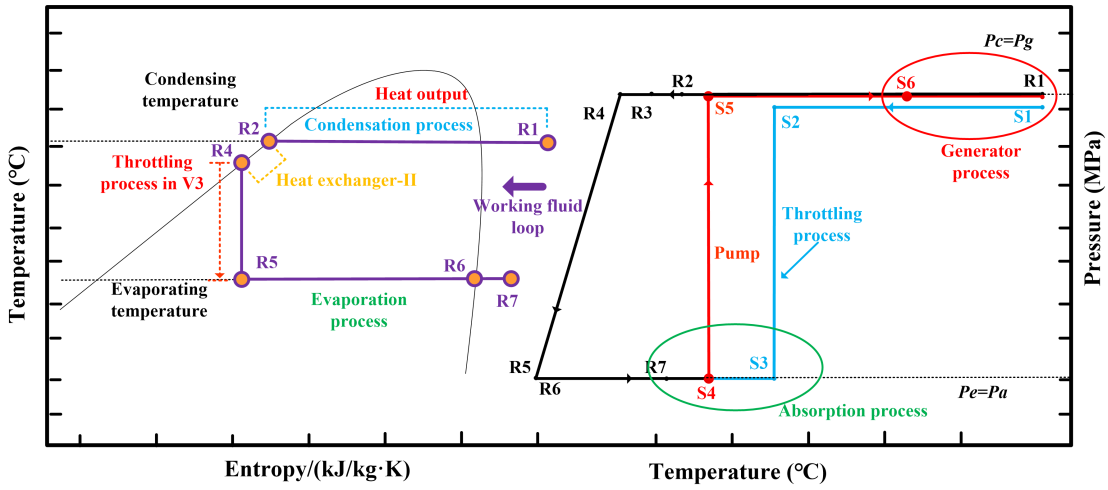


Fig. 3 P-T diagram of the ASAHP system

### 3.1. The coupled model

Solution equilibrium equations and absorption cycle model have been listed in Appendix B. Figs. 4(a) and 4(b) show the diagram of the two-dimensional distributed parameter model for both the absorber and the generator. A fully developed two-phase of R22-DEGDME solution flows downward and the pure R22 gas flows upwards in a copper pipe. The solution film with even inlet temperature and mass fraction goes to the pipe with an initial thickness of $\delta_{l.in}$. In the absorber, the liquid film thickness increases due to the continuous absorption of R22 vapor during the falling film process; while in the generator, the liquid film thickness decreases because of the constant release of R22 vapor during the process. The two-dimensional distributed parameter model is defined in Cartesian coordinates, and x represents the pipe length direction and y represents the pipe diameter direction, respectively.

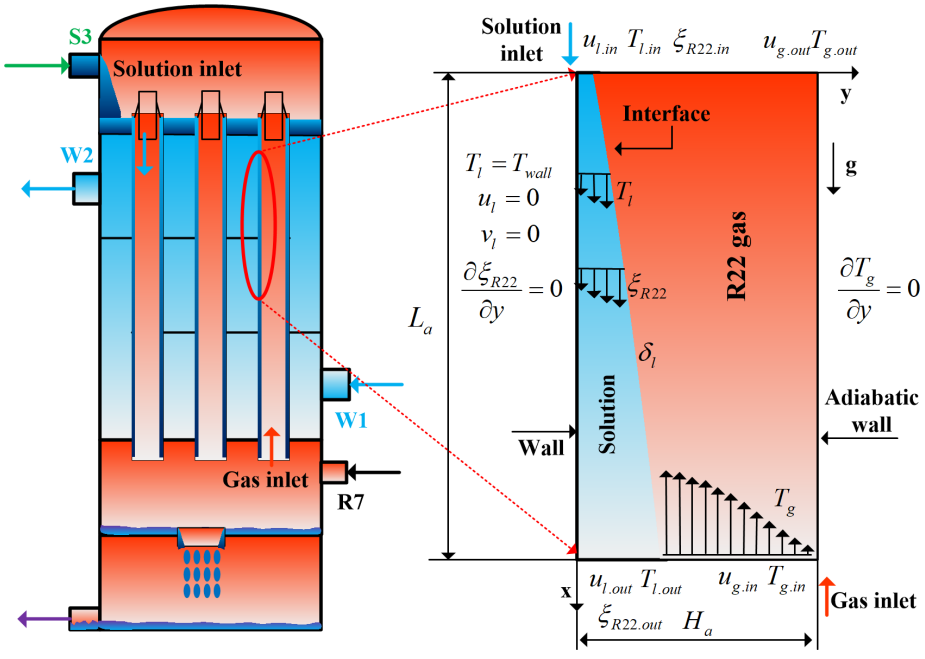

(a) absorber

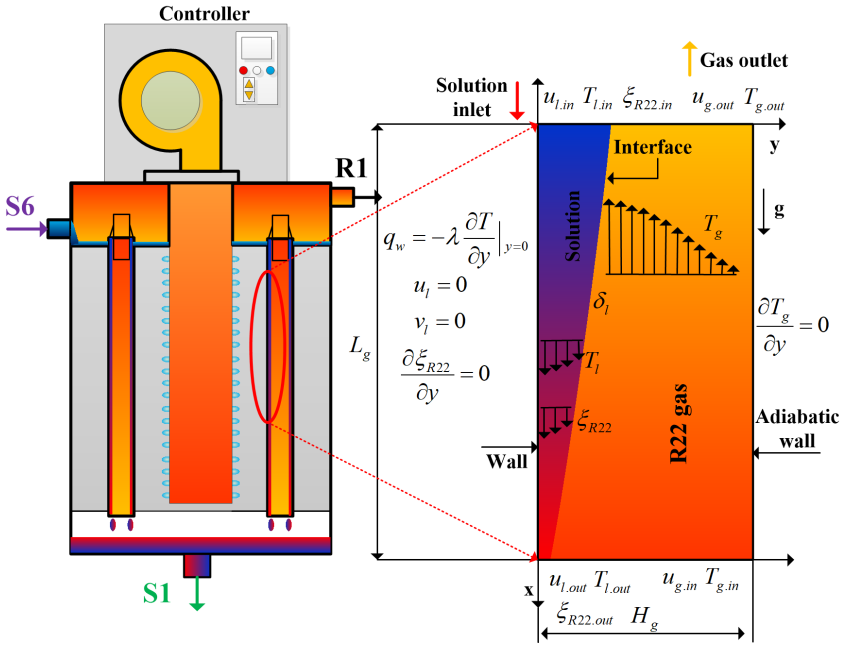


(b)Generator

Fig.4 Domain definition and boundary conditions for two-phase absorption in two phase absorption and generation

In the absorber and the generator, the governing equations of energy, mass, and momentum are listed as follows. In the liquid phase, the mass balance equations of liquid is governed by Equation 6,

$$\frac{\partial \rho_l}{\partial \tau} + \frac{\partial (\rho_l u_l)}{\partial x} + \frac{\partial (\rho_l v_l)}{\partial y} = 0 \tag{6}$$

In both x and y directions, the momentum equation in the liquid phase can be described by Equations 7 and 8,

$$\frac{\partial (\rho_l u_l)}{\partial \tau} + \frac{\partial (\rho_l u_l u_l)}{\partial x} + \frac{\partial (\rho_l v_l u_l)}{\partial y} = -\frac{\partial P_l}{\partial x} + \mu_l \left(\frac{\partial^2 u_l}{\partial x^2} + \frac{\partial^2 u_l}{\partial y^2}\right) + \rho_l g_x \tag{7}$$

$$\frac{\partial (\rho_l v_l)}{\partial \tau} + \frac{\partial (\rho_l u_l v_l)}{\partial x} + \frac{\partial (\rho_l v_l v_l)}{\partial y} = -\frac{\partial P_l}{\partial y} + \mu_l \left(\frac{\partial^2 v_l}{\partial x^2} + \frac{\partial^2 v_l}{\partial y^2}\right) + \rho_l g_y \tag{8}$$

In the solution energy conservation equations, the energy transfer due to

inter-diffusion should be considered in the energy balance equation. The energy conservation equation of the liquid solution is written as Equation 9,

$$\frac{\partial(\rho_l c_{p.l} T_l)}{\partial \tau} + \frac{\partial(\rho_l c_{p.l} u_l T_l)}{\partial x} = \lambda_l \left(\frac{\partial^2 T_l}{\partial x^2} + \frac{\partial^2 T_l}{\partial y^2}\right) + \rho_l D_l \frac{\partial^2 \xi_{R22}}{\partial y^2} (\bar{h}_{R22} - \bar{h}_{DEG}) \quad (9)$$

As there is no concentration equation for pure vapor, the R22 component equilibrium equation in the liquid phase can be defined by Equation 10,

$$\frac{\partial(\rho_l \xi_{R22})}{\partial \tau} + \frac{\partial(\rho_l u_l \xi_{R22})}{\partial x} + \frac{\partial(\rho_l v_l \xi_{R22})}{\partial y} = \rho_l D_l \left(\frac{\partial^2 \xi_{R22}}{\partial x^2} + \frac{\partial^2 \xi_{R22}}{\partial y^2}\right) \quad (10)$$

In the gas phase, mass, momentum, and energy conversation equations are described by Equations 11-14,

$$\frac{\partial \rho_g}{\partial \tau} + \frac{\partial(\rho_g u_g)}{\partial x} + \frac{\partial(\rho_g v_g)}{\partial y} = 0 \quad (11)$$

$$\frac{\partial(\rho_g u_g)}{\partial \tau} + \frac{\partial(\rho_g u_g u_g)}{\partial x} + \frac{\partial(\rho_g v_g u_g)}{\partial y} = -\frac{\partial P_g}{\partial x} + \mu_g \left(\frac{\partial^2 u_g}{\partial x^2} + \frac{\partial^2 u_g}{\partial y^2}\right) + \rho_g g_x \quad (12)$$

$$\frac{\partial(\rho_g v_g)}{\partial \tau} + \frac{\partial(\rho_g u_g v_g)}{\partial x} + \frac{\partial(\rho_g v_g v_g)}{\partial y} = -\frac{\partial P_g}{\partial y} + \mu_g \left(\frac{\partial^2 v_g}{\partial x^2} + \frac{\partial^2 v_g}{\partial y^2}\right) + \rho_g g_y \quad (13)$$

$$\frac{\partial(\rho_g c_{p.g} T_g)}{\partial \tau} + \frac{\partial(\rho_g c_{p.g} u_g T_g)}{\partial x} + \frac{\partial(\rho_g c_{p.g} v_g T_g)}{\partial y} = \lambda_g \left(\frac{\partial^2 T_g}{\partial x^2} + \frac{\partial^2 T_g}{\partial y^2}\right) \quad (14)$$

### 3.2. Boundary conditions

To solve the distributed parameter model mentioned above, the boundary conditions for the model are necessary. Firstly, some assumptions were made:

1) The velocity in the y direction is ignored (M.Mittermaier et al. 2015).
2) The velocity of solution and vapor in the x direction is constant (M.Mittermaier et al. 2015).
3) The solution is an in-compressible and the film thickness is constant

(Mittermaier et al. 2014).

4) The convection term in the y direction and the diffused term in the x direction is neglected (E.García-Rivera et al. 2019).

5) The wall temperature of the absorber and the heat flux density in the generator is constant (Robabeh et al. 2018).

According to Figs. 4(a) and 4(b), the boundary conditions were defined. At the inlet of the absorber and the generator (x=0), the inlet temperature, velocity and mass fraction of R22 are given by Equations 15 and 16,

$$u_{l.in}=u,\ T_{l.in}=T_{S3},\ \xi_{R22.in}=\xi_{R22.S3},\ \frac{\partial T_g}{\partial x}=0 \qquad \text{Absorber} \qquad (15)$$

$$u_{l.in}=u,\ T_{l.in}=T_{S6},\ \xi_{R22.in}=\xi_{R22.S6},\ \frac{\partial T_g}{\partial x}=0 \qquad \text{Generator} \qquad (16)$$

At the wall beside the liquid phase (y=0), the conditions for wall temperature, velocity and mass fraction of R22 are given. The wall liquid temperature equals to the pipe wall temperature in the absorber; while the pipe wall is defined by the second type of boundary conditions in the generator. The mass fraction gradient at the wall is 0 as there is no mass transfer.

$$u_l=0,\ v_l=0,\ T_l=T_{wall},\ \frac{\partial \xi_{R22}}{\partial y}=0 \qquad \text{Absorber} \qquad (17)$$

$$u_l=0,\ v_l=0,\ q_w=-\lambda_l\frac{\partial T_l}{\partial y}\Big|_{y=0},\ \frac{\partial \xi_{R22}}{\partial y}=0 \qquad \text{Generator} \qquad (18)$$

At the wall beside the R22 gas phase (y=$H_a$, $H_g$), the wall with a temperature gradient of 0 is an adiabatic wall.

$$\frac{\partial T_g}{\partial y}=0 \qquad (19)$$

At the outlet of the pipe (x=$L_a$, $L_g$), the boundary conditions are defined as:

$$\frac{\partial T_l}{\partial x}=0,\ \frac{\partial \xi_{R22}}{\partial x}=0,\ u_{g.in}=u_2,\ T_{g.in}=T_{R7} \quad \text{Absorber} \quad (20)$$

$$\frac{\partial T_l}{\partial x}=0,\ \frac{\partial \xi_{R22}}{\partial x}=0,\ u_{g.in}=u_2,\ T_{g.in}=T_{l.out} \quad \text{Generator} \quad (21)$$

At the interface, the temperature is continuous and the solution temperature equals to the vapor temperature. Both absorption heat and generator heat are transferred into the film by the heat conduction.

$$T_{l.\mathrm{int}f}=T_{g.\mathrm{int}f} \quad (22)$$

$$-\lambda_l \frac{\partial T_l}{\partial y}\Big|_{y=\delta}=m_{\mathrm{int}f}\cdot\Delta h \quad (23)$$

where $m_{\mathrm{int}f}$ is the mass flux at the interface and $\Delta h$ is the absorption heat and generator heat which has been defined as a function of the enthalpy of refrigerant vapor and the partial enthalpy of R22 in the solution.

$$m_{\mathrm{int}f}=-\rho_l D_l \frac{\partial \xi_{R22}}{\partial y}\Big|_{y=\delta} \quad (24)$$

$$\Delta h=(h_{R22,g}-\bar{h}_{R22,l})_{\mathrm{int}f} \quad (25)$$

### 3.3. Solution method

For the solution of the coupled model, the specific code was developed through Python. In the distributed parameter model, central difference scheme is applied to discretize the diffusion terms, and first-order upwind difference scheme is applied to discretize convection terms. The flowchart of the distributed parameter model algorithm is shown in Fig. 5.

### 3.4. System multi-objective optimization

According to both experimental and simulation results, with increasing water flow rate, the COP increased while the supply water temperature decreased. Therefore, a system multi-objective optimization method should be conducted as it can help to identify the optimal solution at the same time for the two objectives (Wu et al., 2020). There are two objective functions, which are COP and supply water temperature calculated by the lumped parameter model. The decision variables include water flow rate, generator temperature and condensing temperature which have significant effect on the supply water temperature and COP (Jain et al., 2017).

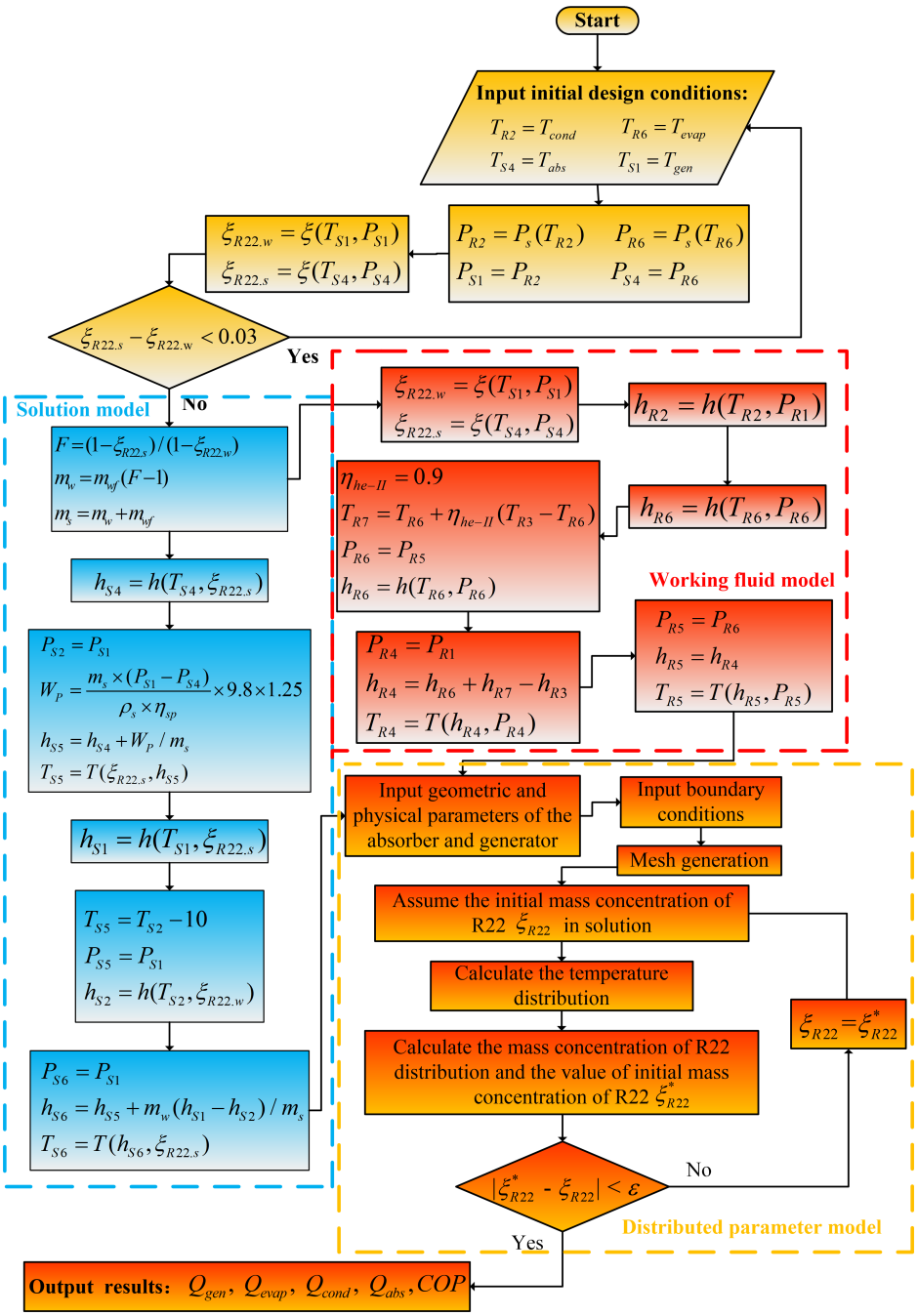


Fig. 5 Flow chart of the distributed parameter model.

The safety operating conditions are applied to formulate the inequality constraints while the lumped parameter model are used to determine the equality constraints. Jain et al., (2017) stated that the NSGA-II approach, a valid evolutive optimization method to find the optimal solutions with the details pseudo codes, can be applied to optimize the decision variables. In addition, Pareto frontier and

TOPSIS decision-making method should also be discussed and adopted (Wang et al., 2017). The non-dimensionalization of both supply water temperature and COP should be conducted by the Fuzzy method (Wu et al., 2019):

$$COP_i^n = \frac{\max(COP_i) - COP_i}{\max(COP_i) - \min(COP_i)} \tag{26}$$

$$T_{w.i}^n = \frac{\max(T_{w.i}) - T_{w.i}}{\max(T_{w.i}) - \min(T_{w.i})} \tag{27}$$

To find the optimized result on the Pareto frontier, the TOPSIS decision-making method has been applied in this study. In this process, there are non-ideal and ideal points, with ideal points maximizing objective functions and non-ideal points minimizing them. On the Pareto frontier, the distance of any points to the ideal and non-ideal points was calculated by Equations 28 and 29 (Wu et al., 2020),

$$d_{i+} = \sqrt{(COP_i - COP^{ideal})^2 + (T_{w.i} - T_w^{ideal})^2} \tag{28}$$

$$d_{i-} = \sqrt{(COP_i - COP^{non-ideal})^2 + (T_{w.i} - T_w^{non-ideal})^2} \tag{29}$$

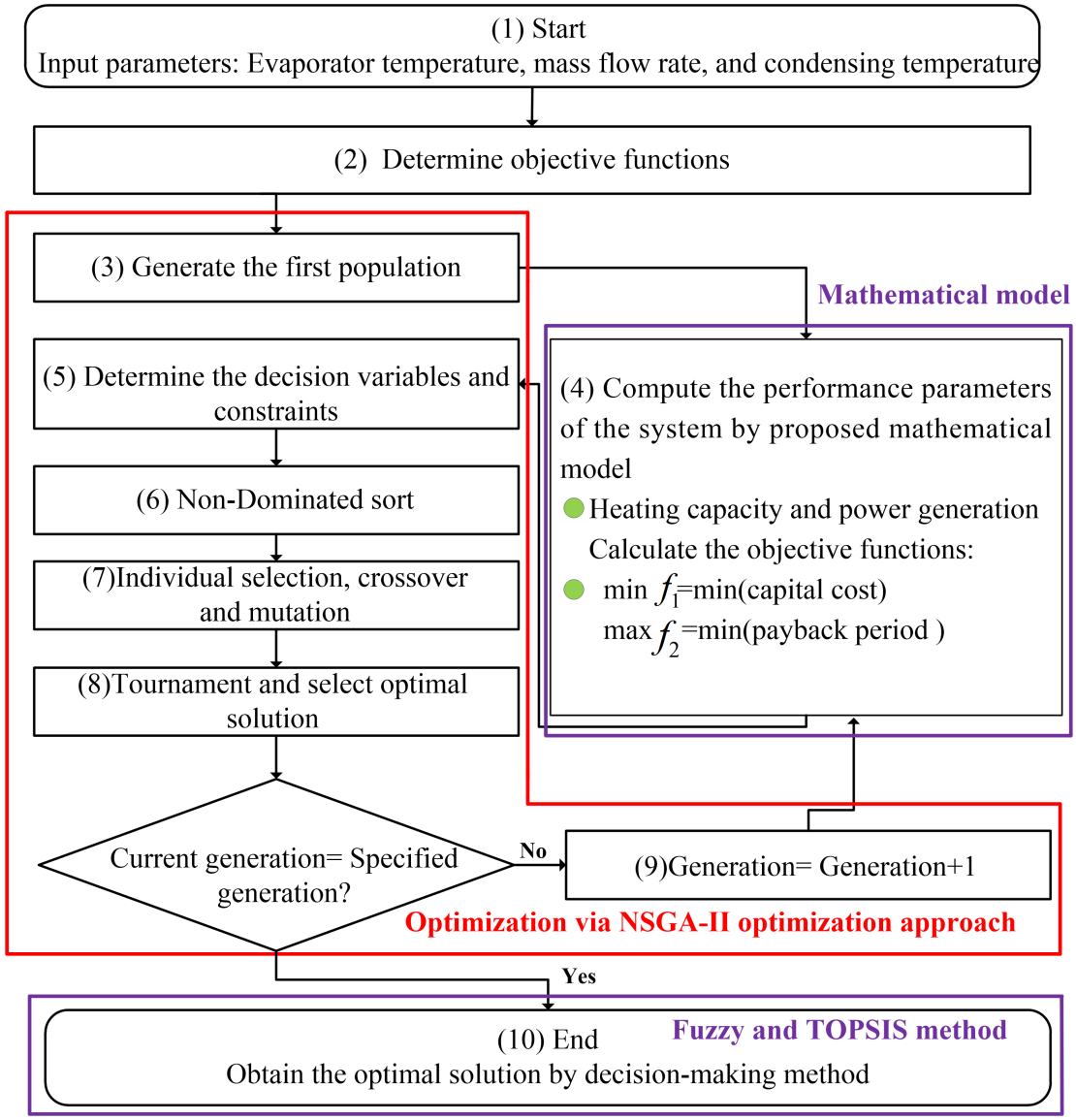


Fig. 6 Flowchart of multi-objective optimization

The proximity index can be calculated by Equation 30 (Wu et al., 2020). The maximum $Cl_i$ is chosen as the final solution and Fig. 6 provides the optimization flow chart.

$$Cl_i = \frac{d_{i-}}{d_{i-} + d_{i+}} \tag{30}$$

## 4. Results and discussions

The generator is heated separately to achieve set conditions as soon as possible, before the system starts. Fig. 7 shows the start-up performance consisting of both pressure and temperature in the generator. As shown in Fig. 7, it took 40 minutes for the solution temperature to increase from 100 ℃ to 190 ℃ and the pressure to rise from 12.75 bar to 17.49 bar. The solution temperature and pressure increased approximately in a linear nature with time. After 15 minutes, fan coils and water pumps started to result in decreased solution temperature and pressure. After 40 minutes, the system achieved the set operating condition.

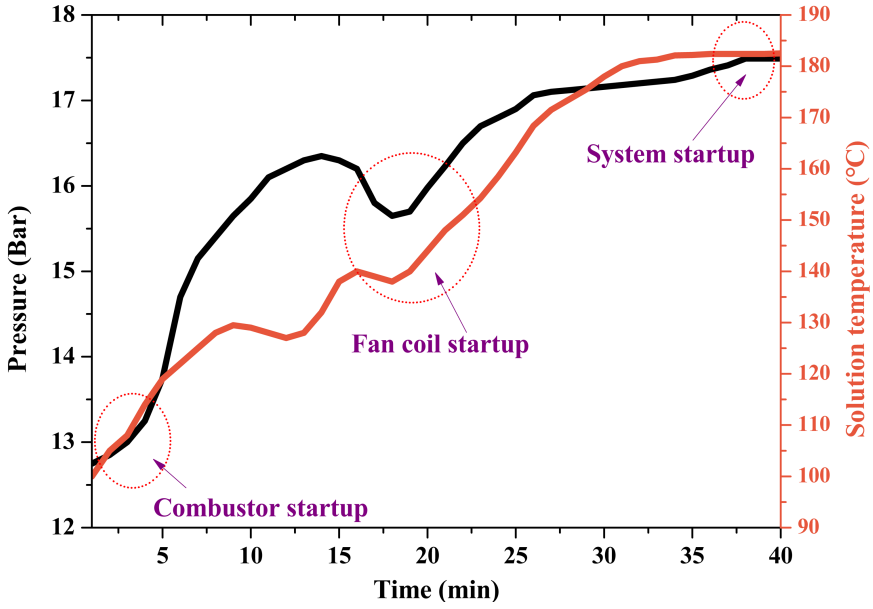


Fig. 7 Starting performance of the system

### 4.1. Thermal performance analysis

At a typical operating condition calculated by the lumped parameters model, Table 3 indicates uncertainty within the system and the experimental parameters. The pressure meter, PT-100, and volume flowmeter have been applied to collect

389 experimental values which are recorded data acquisition machine. The average
390 values are the average of five measurements and the system uncertainty is the error
391 of the device. Table 4 displays the thermodynamic analysis of the heat load and COP
392 under a typical condition. The absorber load, condenser load, evaporator load and
393 generator load calculated by the Equations (B-6)-(B-9) are 11.42 kW, 24.98 kW,
394 14.79 kW and 23.02 kW, respectively. Heating capacity calculated by Equation
395 (B-10) is the sum of the condenser load and absorber load while the COP defined by
396 the Equation (B-13) is 1.58.
397

398 Table 3 Experimental values and the uncertainty of different parameters

| Variables | State points | Average values | System uncertainty |
|---|---|---|---|
| Working fluid temperature in generator outlet | R1 | 191.5 ℃ | ±0.1 ℃ |
| Working fluid temperature in condenser outlet | R2 | 46.3 ℃ | ±0.1 ℃ |
| Working fluid temperature in reservoir outlet | R3 | 46.1 ℃ | ±0.1 ℃ |
| Working fluid temperature in heat exchanger-II outlet | R4 | 25.8 ℃ | ±0.1 ℃ |
| Working fluid temperature in evaporator inlet | R5 | -9.2 ℃ | ±0.1 ℃ |
| Working fluid temperature in evaporator outlet | R6 | -8.9 ℃ | ±0.1 ℃ |
| Working fluid temperature in absorber inlet | R7 | 28.4 ℃ | ±0.1 ℃ |
| Water temperature in absorber inlet | W1 | 24.5 ℃ | ±0.1 ℃ |
| Water temperature in condenser inlet | W2 | 31.3 ℃ | ±0.1 ℃ |
| Supply water temperature | W3 | 38.4 ℃ | ±0.1 ℃ |
| Weak solution temperature in generator outlet | S1 | 190.9 ℃ | ±0.1 ℃ |
| Weak solution temperature in heat exchanger outlet | S2 | 50.8 ℃ | ±0.1 ℃ |

| | | | |
|---|---|---|---|
| Weak solution temperature in absorber inlet | S3 | 48.2 ℃ | ±0.1 ℃ |
| Strong solution temperature in absorber outlet | S4 | 43.5 ℃ | ±0.1 ℃ |
| Strong solution temperature in solution pump outlet | S5 | 44.5 ℃ | ±0.1 ℃ |
| Strong solution temperature in generator inlet | S6 | 131.8 ℃ | ±0.1 ℃ |
| Water flow rate | Flowmeter-IV | 2.3 m³/h | ±0.1 m³/h |
| Working fluid flow rate | Flowmeter-III | 0.25 m³/h | ±0.02 m³/h |
| Strong solution flow rate | Flowmeter-II | 1.71 m³/h | ±0.02 m³/h |
| Weak solution flow rate | Flowmeter-I | 1.38 m³/h | ±0.02 m³/h |
| Natural gas flow rate | Controller | 2.42 m³/h | ±0.02 m³/h |
| Generator pressure | - | 1.85 MPa | ±0.01 MPa |
| Evaporation pressure | - | 0.35 MPa | ±0.01 MPa |

Table 4 Performance analysis of the heat load under a typical condition

| Variables | Values | Accuracy |
|---|---|---|
| Absorber load | 11.42 kW | ±0.42 kW |
| Condenser load | 24.98 kW | ±0.38 kW |
| Evaporator load | 14.79 kW | ±0.42 kW |
| Generator load | 23.02 kW | ±0.43 kW |
| COP | 1.58 | ±0.05 |
| Heating capacity | 36.41 kW | ±0.52 kW |

Fig. 8 depicts the variations of the COP and heating capacity in both experiment and simulation, with rising generator temperature at different evaporation temperatures. In Fig. 8, there are three sets of data which are experimental value, simulation value and simulation value after model correction. The simulation values were calculated according to the lumped parameter model, while simulation values after model correction were calculated based on the coupled model shown in Section 3.1. From Figs. 8(a) and 8(b), all experimental values, simulation values and

409 simulation values after model correction of the heating capacity rose with the
410 increasing generator temperature at the evaporation temperatures of -10 ℃ and -5 ℃.
411 When the generator temperature was 190 ℃, the simulation heating capacity,
412 simulation heating capacity after model correction and the experimental heating
413 capacity were 37.77 kW, 36.75 kW and 36.41 kW, respectively, at the evaporation
414 temperature of -10 ℃; while they were 46.51 kW, 44.65 kW and 44.98 kW, when the
415 evaporation temperature was -5 ℃. Relative errors of experimental heating capacity
416 to simulation heating capacity and simulation heating capacity after model correction
417 were 3.61% and 2.69% at the evaporation temperatures of -10 ℃, and they were
418 3.99% and 3.27% at the evaporation temperatures of -5 ℃. It could be observed in
419 Figs. 8(c) and 8(d) that with the increase of generator temperature, the COP
420 increased at both evaporation temperatures of -10 ℃ and -5 ℃. At the generator
421 temperature of 190 ℃, the simulated COP was 1.66, simulated COP after model
422 correction was 1.61 and the experimental COP was 1.58, at the evaporation
423 temperature of -10 ℃, and they were 1.64, 1.66 and 1.71, when the evaporation
424 temperature was -5 ℃. Under this condition, the relative errors of experimental COP
425 to simulated COP and simulated COP after model correction were 4.47% and 2.73%
426 at the evaporation temperatures of -10 ℃, and they were 4.03% and 3.11% at the
427 evaporation temperature of -5 ℃. These trends can be interpreted that increasing
428 generator temperature causes decreasing weak solution concentration. If the strong
429 solution concentration determined by the evaporation temperature keeps unchanged,
430 the deflation ratio will rise leading to the increasing absorption ability. Furthermore,

the working fluid mass flow rate increased which caused the increase of both heating capacity and COP. In addition, the increase of evaporation temperature caused the increase of absorber pressure, leading to an increase of strong solution concentration. If the weak solution concentration determined by the generator temperature was unchanged, the deflation ratio would rise, leading to the increase of absorption ability. The experimental value was lower than the simulated value, and this is because there were pressure and heat loss under the experimental conditions.

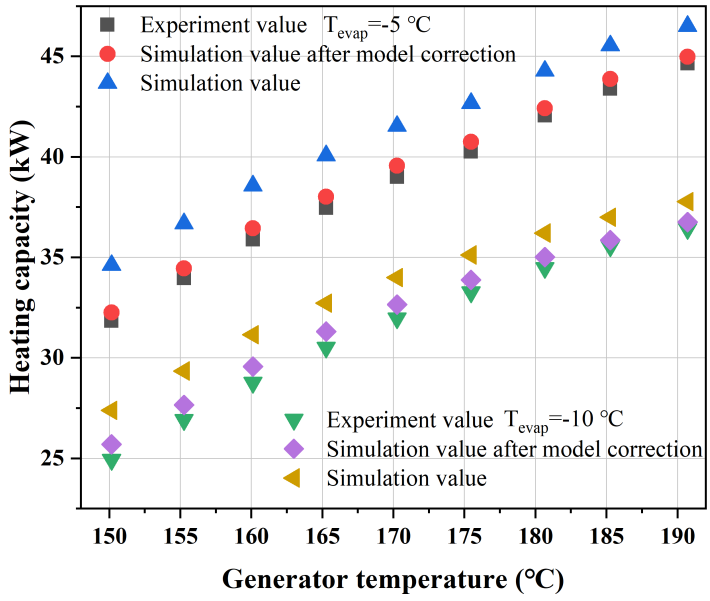


(a)

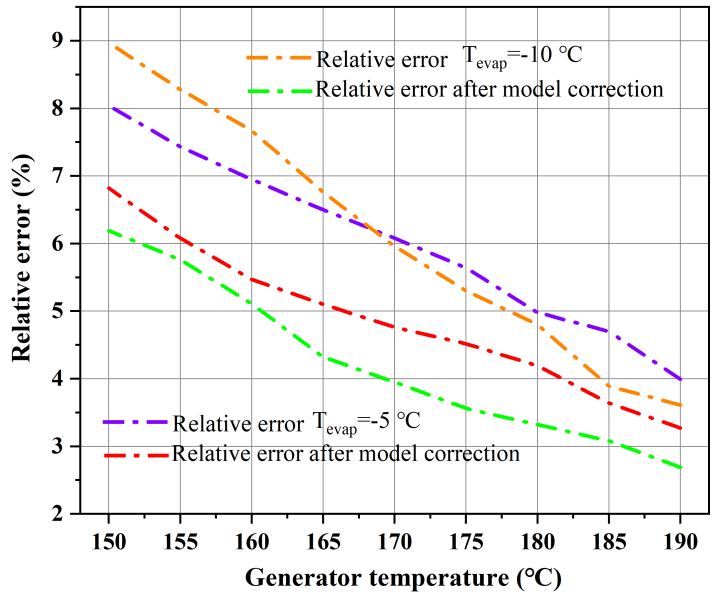


441

442 (b)

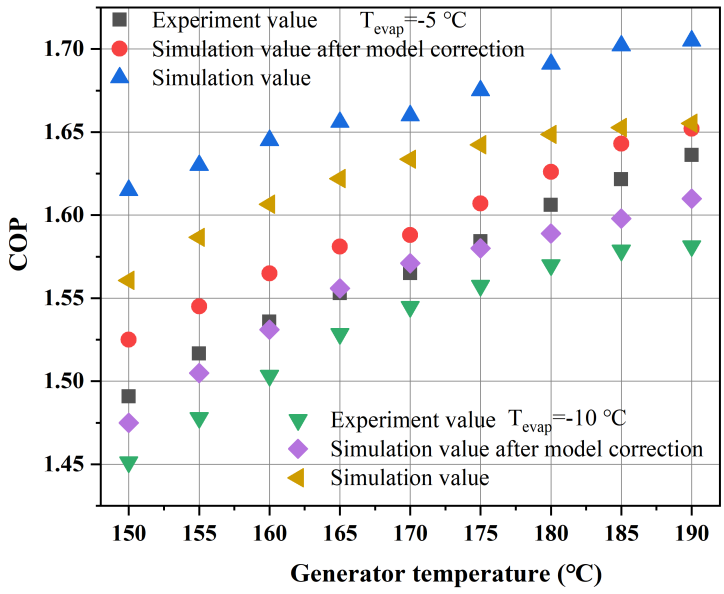


443

444 (c)

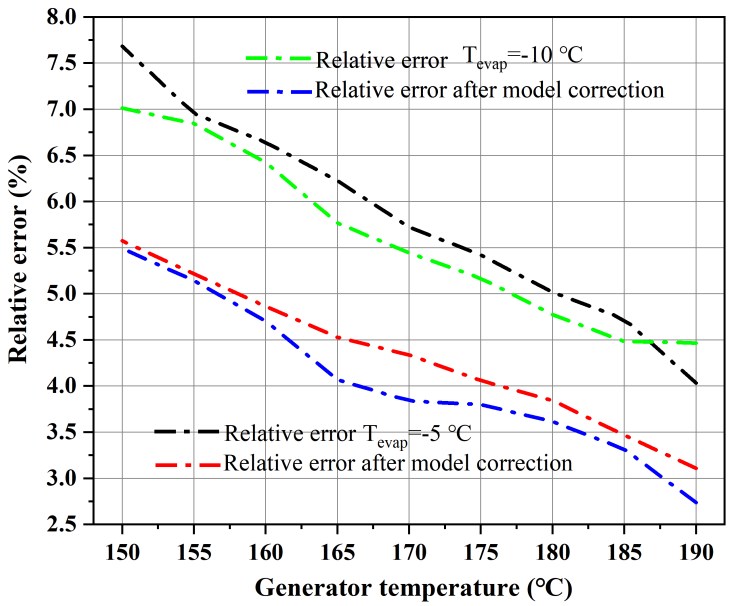


(d)

Fig. 8 Variation of COP and heating capacity under different generator and evaporation temperature

Fig. 9 illustrates the variation of heating capacity and COP at different condensing and evaporation temperature. It can be seen from the Figs. 9(a) and 9(c), the heating capacity decreased with the rising condensing temperature at the different evaporation temperature. When the condensing temperature was 46.5 ℃, the simulation and experiment heating capacity were minimized; the simulation heating capacity, simulation heating capacity after model correction and experiment heating capacity were 39.13 kW, 35.65 kW and 36.41 kW with the relative error of 3.69% and 2.74% at the evaporation temperature of -10 ℃; these heating capacity were 48.55 kW, 44.65 kW and 44.85 kW with the relative error of 3.41% and 2.86% at the evaporation temperature of -5 ℃. Figs. 9(b) and 9(d) indicate the COP decreased with the increasing condensing temperature. The COP reached minimum value at the condensing temperature of 46.5 ℃; the simulation COP, simulation COP

462 after model correction and experiment COP were 1.58, 1.48 and 1.44 with the
463 relative error of 4.46% and 2.74%, respectively, when the evaporation temperature
464 was -10 ℃; the simulation COP, simulation COP after model correction and
465 experiment COP were 1.62, 1.52 and 1.48 with the relative error of 4.03% and
466 2.64%, respectively, at the evaporation temperature of -5 ℃. This could be explained
467 by that the increase of condensing temperature resulted in a growing working fluid
468 enthalpy in the condenser outlet which would lead to the decrease of COP and
469 heating capacity.

470

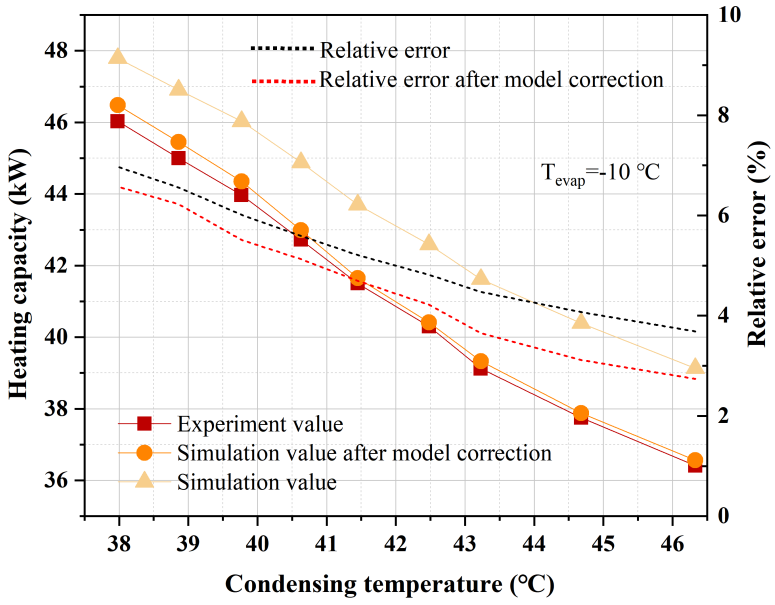


471

472 (a)

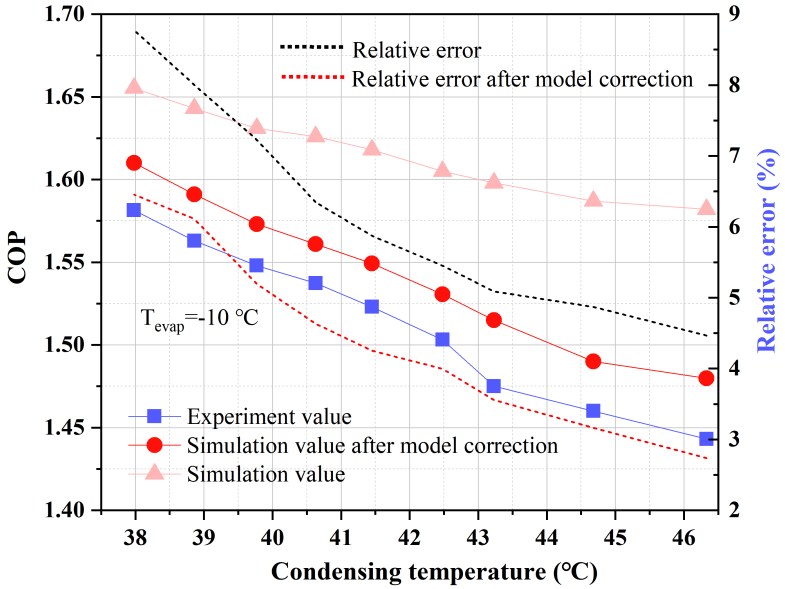


473

474 (b)

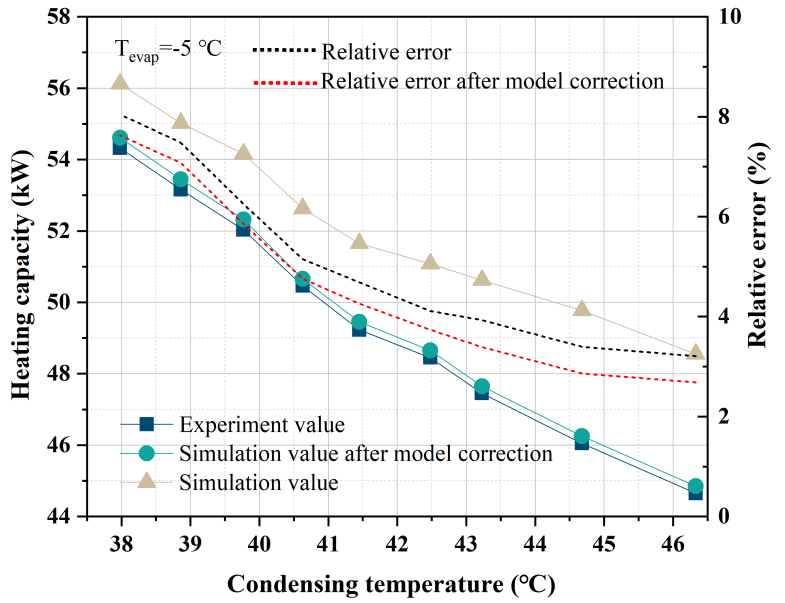


475

476 (c)

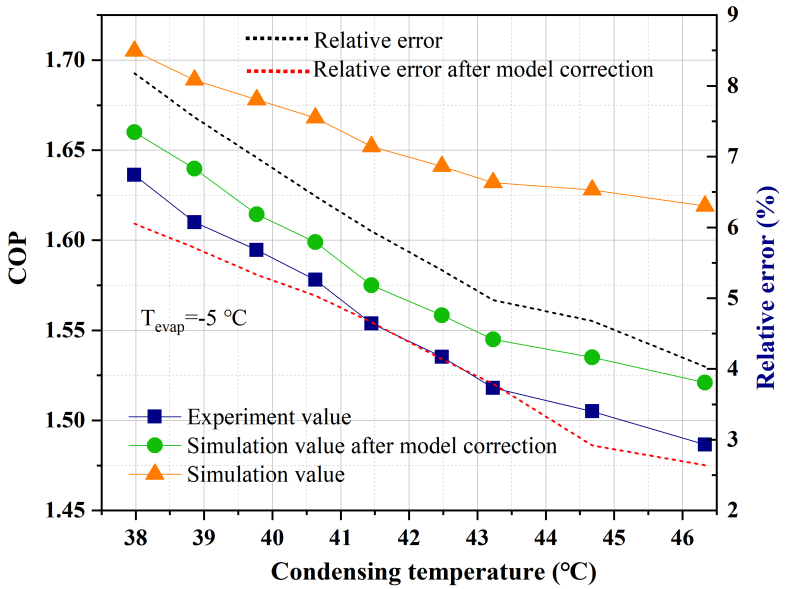


(d)

Fig. 9 Variation of COP and heating capacity under different condensing and evaporation temperature

Fig. 10 presents the change of COP and supply water temperature with different flow rate of water. It can be seen that with the rising flow rate of water, the COP rose but the supply water temperature decreased. Fig. 10 illustrates that while the flow rate of water was 2.25 m³/h, the COP was 1.58 and the supply water temperature was 38.8 ℃; while the flow rate of water increased from 2.25 m³/h to 6.98 m³/h, the COP increased from 1.58 to 1.66 while the supply water temperature decreased from 38.8 ℃ to 30.6 ℃. This could be explained by that the increase of water flow rate caused the reducing condensing temperature which leading to the increase of refrigerant enthalpy difference in the condenser inlet and outlet. This would lead to the increase of heating capacity and COP, when the working fluid mass flow rate kept unchanged.

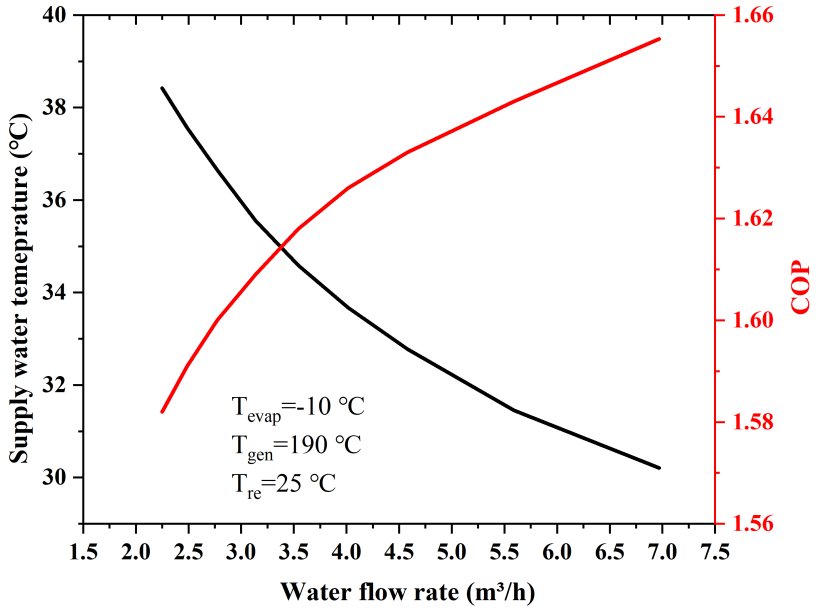


Fig. 10 Variation of supply water temperature and COP with the increase of water flow rate

## 4.2. Coupled model validation

The coupled model should be validated to ensure its accuracy and correctness. Table 5 shows the comparison between experimental values and simulated values after model correction in the generator. It is shown that the maximum relative error of $T_{R1\text{-}Ex}$ and $T_{R1\text{-}Sim}$ was 3.12%, while the maximum relative error of $T_{S1\text{-}Ex}$ and $T_{S1\text{-}Sim}$ was 4.75%. Table 6 displays the comparison between experimental values and simulated values in the absorber. It shows the maximum relative error of $T_{S4\text{-}Ex}$ and $T_{S4\text{-}Sim}$ of 5.03%. The simulated solutions were in good agreement with the experimental results under the condition of the necessary assumptions and instrument errors. In addition, the distributed parameter model can be used to predict the thermal performance of both generators and absorbers.

Table 5 Experimental values and simulation values in generator under different conditions

| $T_{evap}$ | Case | $T_{W1}$ (℃) | $T_{W3}$ (℃) | $T_{S6}$ (℃) | $T_{R1\text{-}Sim}$ (℃) | $T_{R1\text{-}Ex}$ (℃) | RE (%) | $T_{S1\text{-}Sim}$ (℃) | $T_{S1\text{-}Ex}$ (℃) | RE (%) |
|---|---|---|---|---|---|---|---|---|---|---|

| | | | | | | | | | | |
|---|---|---|---|---|---|---|---|---|---|---|
| $T_{evap}$= -10 ℃ | 1 | 24.5 | 38.4 | 131.1 | 193.1 | 190.3 | 1.47 | 195.7 | 190.6 | 2.71 |
| | 2 | 24.5 | 37.9 | 129.4 | 187.8 | 184.8 | 1.58 | 190.8 | 185.1 | 3.06 |
| | 3 | 24.5 | 37.5 | 127.7 | 183.3 | 180.2 | 1.73 | 186.4 | 180.2 | 3.41 |
| | 4 | 24.6 | 37.1 | 126.1 | 178.8 | 175.1 | 2.16 | 181.1 | 175.1 | 3.48 |
| | 5 | 24.6 | 36.6 | 124.5 | 174.1 | 169.8 | 2.50 | 176.9 | 170.1 | 3.96 |
| | 6 | 24.6 | 36.3 | 123.1 | 169.4 | 164.8 | 2.75 | 172.3 | 165.2 | 4.33 |
| | 7 | 24.6 | 35.9 | 121.6 | 164.4 | 159.7 | 2.93 | 167.1 | 159.9 | 4.39 |
| | 8 | 24.6 | 35.6 | 120.2 | 159.5 | 154.9 | 3.05 | 162.3 | 155.1 | 4.60 |
| | 9 | 24.6 | 34.9 | 119.1 | 154.4 | 149.7 | 3.12 | 157.2 | 150.1 | 4.75 |
| $T_{evap}$= -5 ℃ | 10 | 24.4 | 39.7 | 122.1 | 193.2 | 190.2 | 1.59 | 192.5 | 190.2 | 1.23 |
| | 11 | 24.5 | 39.3 | 120.4 | 189.3 | 184.7 | 2.52 | 187.3 | 184.7 | 1.42 |
| | 12 | 24.5 | 38.9 | 118.9 | 184.1 | 180.1 | 2.24 | 182.7 | 180.1 | 1.46 |
| | 13 | 24.5 | 38.5 | 117.4 | 178.2 | 174.9 | 1.88 | 177.5 | 174.9 | 1.49 |
| | 14 | 24.5 | 38.1 | 115.9 | 172.4 | 169.7 | 1.62 | 172.5 | 169.7 | 1.68 |
| | 15 | 24.5 | 37.7 | 114.6 | 166.9 | 164.7 | 1.36 | 167.9 | 164.8 | 1.94 |
| | 16 | 24.5 | 37.3 | 113.3 | 163.8 | 159.5 | 2.67 | 162.7 | 159.5 | 1.99 |
| | 17 | 24.5 | 37.0 | 112.1 | 158.5 | 154.7 | 2.45 | 158.1 | 154.7 | 2.17 |
| | 18 | 24.5 | 36.3 | 110.9 | 153.1 | 149.6 | 2.32 | 153.4 | 149.6 | 2.53 |

Table 6 Experimental values and simulation values in absorber under different conditions

| $T_{evap}$ | Case | $T_{W1}$ (℃) | $T_{W3}$ (℃) | $T_{S3}$ (℃) | $T_{R7}$ (℃) | $T_{S4\text{-}Sim}$ (℃) | $T_{S4\text{-}Ex}$ (℃) | RE (%) |
|---|---|---|---|---|---|---|---|---|
| $T_{evap}$= -10 ℃ | 1 | 24.5 | 38.4 | 48.5 | 24.8 | 43.5 | 41.9 | 3.73 |
| | 2 | 24.5 | 38.1 | 47.5 | 27.6 | 41.3 | 39.7 | 3.92 |
| | 3 | 24.5 | 37.9 | 46.5 | 26.9 | 40.5 | 38.9 | 3.96 |
| | 4 | 24.5 | 37.8 | 45.5 | 26.2 | 39.8 | 38.3 | 3.99 |
| | 5 | 24.5 | 37.7 | 44.5 | 25.5 | 38.7 | 37.2 | 4.18 |
| | 6 | 24.5 | 37.6 | 43.5 | 24.8 | 37.2 | 35.6 | 4.44 |
| | 7 | 24.5 | 37.6 | 42.5 | 24.1 | 36.2 | 34.6 | 4.49 |
| | 8 | 24.5 | 37.5 | 41.5 | 23.4 | 35.3 | 33.7 | 4.67 |
| | 9 | 24.5 | 37.4 | 40.4 | 22.7 | 34.6 | 33.1 | 5.03 |

### 4.3. Performance analysis in both absorbers and generators

Fig. 11 shows the interface temperature and mass concentration in both generators and absorbers, according to the distributed parameter model described in

513 Section 3.2. It is shown in Fig. 11(a) that the interface temperature decreased slowly
514 in the initial part of the pipe and dropped rapidly after 300 mm. This is because that
515 in the initial stage, the solution concentration is low and the ability to absorb steam is
516 strong; more absorbed heat is released when the R22 vapor is absorbed, leading to
517 little change in interface temperature. Then, the rising mass fraction of the solution
518 leads to the gradual decrease of absorptive capacity and the conductive heat transfer
519 rate through the wall becomes greater than the absorption heat. Therefore, the
520 interface temperature gradually decreases and basically reaches the same
521 temperature as the wall temperature at the pipe exit. The variation trend of interface
522 mass concentration is opposite to that of interface temperature. Fig. 11(a) indicates
523 that the interface temperature increased rapidly in the initial part of the pipe and
524 reached 190 ℃ at 200 mm. After 200 mm, the interface temperature remained
525 almost constant. This is because at the inlet, the solution temperature is low and the
526 R22 mass concentration is high; the heat released by the combustor is partly given to
527 the solution, and partly to generating heat of the refrigerant. And the interface
528 temperature is lower, releasing less refrigerant vapor. When the solution temperature
529 reached 190 ℃, the heat released by the combustor provided the generating heat for
530 the refrigerant leading to the constant interface temperature. According to a reference
531 (Robabeh et al., 2020), a two-dimensional numerical model of a vertical falling film
532 absorber was proposed, and their results showed that the interface temperature
533 decreased while the interface mass concentration increased with the increasing tube
534 length, which is similar to the results from the proposed model .

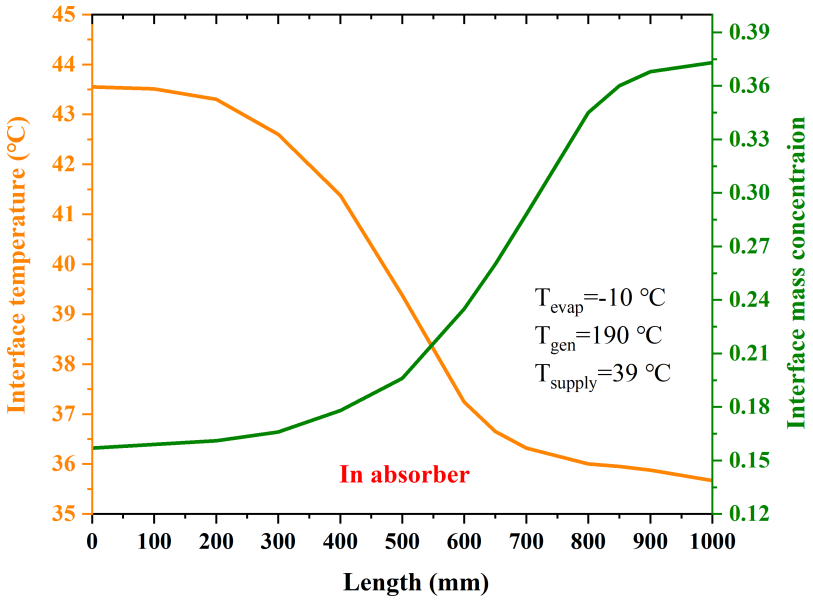


(a)

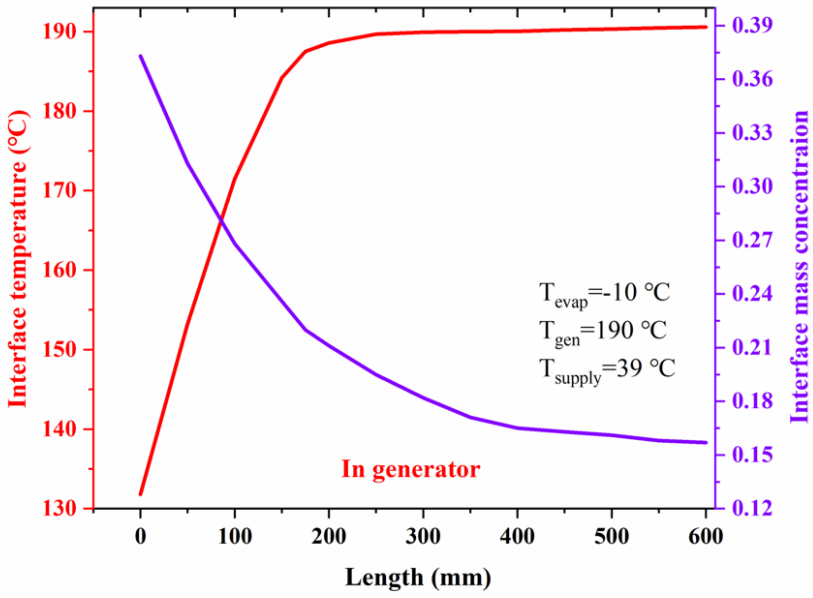


(b)

Fig. 11 Interface temperature and mass concentration in the generator and absorber

### 4.4. System optimization

It can be seen from Fig. 10 that the COP increased but the water supply temperature reduced, with the growing flow rate of water. Under the same evaporation and generation temperature, the higher the COP, the lower the water

supply temperature, and vice versa. According to the NSGA-II approach and TOPSIS decision-making method, the multi-objective optimization elaborated in Section 3.6 is carried out in this study. Table A3 displays the optimization process tuning parameters, and these parameters have been used in a similar study as well (Jain et al., 2017).

According to Equations 26 and 27, the normalized COP and the normalized supply water temperature on the Pareto frontiers optimized by the NSGA-II approach are both displayed in Fig. 12. The supply water temperature and the COP will be maximum at normalized supply water temperature and COP of 1. However, the non-ideal points can be determined at the normalized supply water temperature and COP are 0. In fact, there is no i non-ideal and deal points. While the normalized supply water temperature is 1 and the normalized COP is 0, the system will be optimally designed based on supply water temperature. When the normalized supply water temperature is 0 and the normalized COP is 1, however, the system can be optimally designed based on COP. To find the optimal result on the Pareto frontier, therefore, the TOPSIS decision-making method was applied.

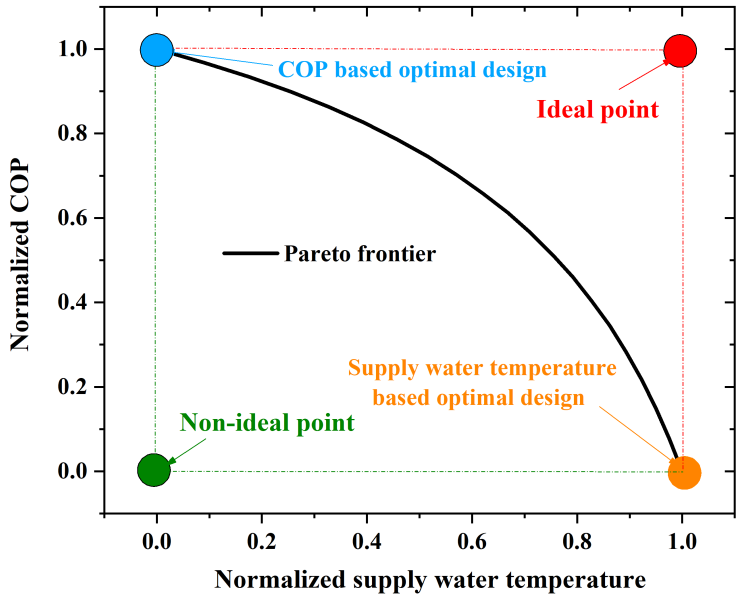


562

563 Fig. 12 Pareto frontier in optimization

564 According to Equations 28-30, $d_{i+}$, $d_{i-}$ and $Cl_i$ was calculated and the

565 maximum $Cl_i$ was chosen as the final result of the proposed system. The variations

566 of $d_{i+}$, $d_{i-}$ and $Cl_i$ with normalized supply water temperature are presented in

567 Fig. 13. From Fig. 13, when the maximum $Cl_i$ was 0.761, the normalized supply

568 water temperature was 0.678. Under this optimal result, the COP was 1.63 with the

569 supply water temperature of 36.3 ℃. It can be seen from Fig. 13 that the system had

570 better COP performance on the left hand side of the orange line while it had better

571 supply water temperature on the right hand side.

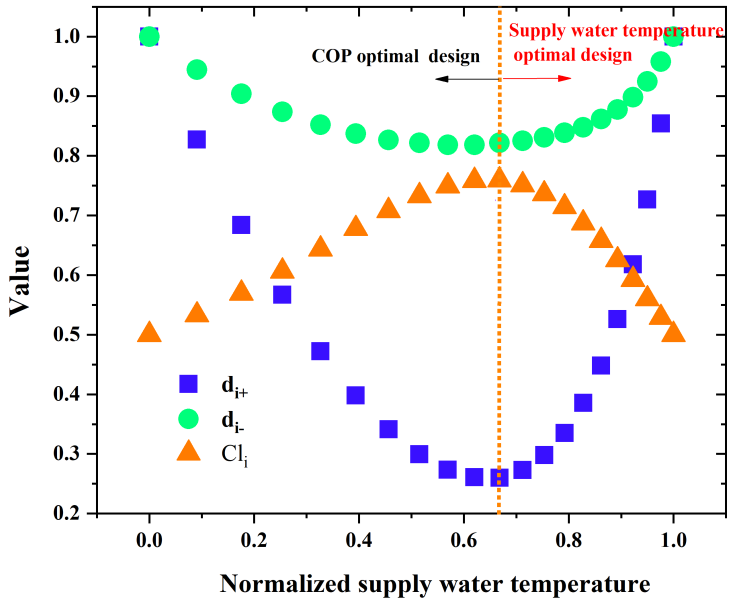


Fig. 13 The distance values and proximity index calculated by the TOPSIS method

Table 7 presents the normalized supply water temperature, the supply water temperature, the normalized COP and the COP in different optimization cases. The results showed that if the system design only considered the COP, the design scheme cannot fully meet the water supply temperature design, and vice versa. If the optimized COP system was chosen, the supply water temperature was 20.98% lower than the maximum possible solution. If the optimized supply water temperature system was determined, the COP was 4.24% lower than its maximum possible solution. However, the COP and supply water temperature were 1.21% and 5.95% lower than their maximized values as the multi-objective optimization design was chosen. Therefore, the multi-objective optimization result can be considered as the optimized working condition.

Under the optimal operating conditions, the multi-objective optimization COP is 1.63 and the supply water temperature is 36.3 ℃ at the evaporation temperature -10 ℃. Lu et al. (2020) have proposed an air-source AHP for heating. They indicated

588 that the system had 30kW heating capacity and the water could be heated from
589 34.2 ℃ to 55.1 ℃ with the COP of 1.66 at the evaporation temperature of 0 ℃.
590 When evaporation temperatures increased from to -10 ℃ to -5 ℃, the COP
591 increased from 1.40 to 1.51, respectively. It can be seen that the COP in this study is
592 higher than the COP in reference (Lu et al., 2020) under the evaporation temperature
593 -10 ℃. This can be explained by that the system in this study has a low condensation
594 temperature (46.3 ℃) and the heat recovery of flue gas.

595 Table 7 Values under different optimization process

| Parameters | COP | Supply water temperature (℃) | Normalized COP | Normalized supply water temperature |
|---|---|---|---|---|
| COP optimal design | 1.65 | 30.5 | 1 | 0 |
| Supply water temperature optimal design | 1.58 | 38.6 | 0 | 1 |
| Multi-objective optimization design | 1.63 | 36.3 | 0.621 | 0.678 |

## 5. Conclusions

In this study, a novel air-source gas-fired absorption heat pump system with vertical falling film exchangers has been proposed for heating buildings. A coupled model was established and a testing rig was built up. The effects of different operating parameters were studied and analyzed. Multi-objective optimization was carried out to find the optimized working conditions. The following main conclusions could be drawn from this study:

1. The proposed system had good stability and feasibility. With the evaporator temperature increasing from -10 ℃ to -5 ℃, the experimental coefficient of performance increased from 1.58 to 1.64, and experimental heating capacity rose from 36.41 kW to 44.98 kW.
2. The proposed coupled model with a maximum error less than 8% is more accurate than the lumped parameter model with a maximum error less than 10%.
3. The variation trend of interface temperature was opposite to that of interface mass concentration in the absorber and generator. The absorber required longer pipes while the generator required more tubes.
4. Under the multi-objective optimization condition, the supply water temperature was 5.95% lower than the maximum values and COP was 1.21% lower than the maximum values which were better than that of single-objective optimization.

This study has fulfilled the gap of improving the use of outdoor heat for heating buildings in cold region, through a novel air-source gas-fired absorption heat pump

system. The proposed system can greatly extend the applications of absorption heat pumps in the district heating and the vertical falling film exchangers can promote the development of this technology. In the future, the stability and compatibility of the ASAHP system with the optimal operating condition should be tested by engineering in cold region. Further research should include the heat exchanger optimization and the new environmental working fluid pair.


## Acknowledgement

This work was supported by the National Key R&D Program of China (No. No. 2020YFD110030)


## Appendix A

The tables for this article are shown below.

Table A1 R22-DEGDME solution properties (Wu et al., 2020)

| Parameters | DEGDME | R22 |
|---|---|---|
| Corrosivity | No | No |
| Toxicity | No | No |
| Density (kg/m$^3$) (t=20 ℃) | 944 | 1210 |
| Critical temperature (℃) | 328.85 | 96.15 |
| Boiling point (℃) (P=101325 Pa) | 162 | -40.8 |
| Molecular weight (g/mol) | 134.17 | 86.46 |

Table A2 Coefficients in Equations.(B-1)-(B-4) (Wu et al., 2020)

| n | $A_n$ | $B_n$ | $C_n$ | $A_n^{c_p}$ | $B_n^{c_p}$ | $C_n^{c_p}$ | $G_n$ |
|---|---|---|---|---|---|---|---|
| 0 | 5.21E+01 | -5.58E+03 | -6.34E+00 | 2.79E+02 | -4.2E-02 | 2.31E-03 | -1.90E+04 |
| 1 | 1.27E+01 | 3.39E+03 | -1.43E+00 | -1.51E+02 | 5.98E-01 | -5.97E-03 | 8.72E+03 |
| 2 | -1.39E+02 | -8.60E+03 | 2.23E+01 | 1.01E+02 | -1.37E+00 | 3.43E-03 | -1.39E+03 |
| 3 | 7.32E+02 | -3.16E+03 | -1.14E+02 | -1.28E+02 | 1.02E+00 | 1.05E-03 | -6.42E+02 |
| 4 | -1.19E+03 | 3.04E+04 | 1.81E+02 | - | - | - | - |
| 5 | 5.47E+02 | -1.90E+04 | -8.19E+01 | - | - | - | - |

Table A3 Multi-objective optimization tuning parameters (Jain et al., 2017)

| Tuning parameters | Value |
|---|---|
| Probability of mutation | 0.9 |
| Maximum number of generations | 400 |
| Population size | 100 |
| Tournament size | 2 |
| Selection process | Tournament |
| Probability of crossover | 0.75 |

## Appendix B

Solution equilibrium equations and absorption cycle model in this study.

According to literature (Takcshito et al., 1984), the solution equilibrium equation consists of three aspects which are solution pressure $P$, molar concentration $Y$ of R22 and solution temperature $T$. It can be defined by Equation B-1,

$$\ln P = \sum_{n=0}^{5} A_n Y^n + \frac{1}{T}\sum_{n=0}^{5} B_n Y^n + \ln T \cdot \sum_{n=0}^{5} C_n Y^n \tag{B-1}$$

The R22-DEGDME solution specific heat composes of R22 molar the solution temperature $T$ and concentration $Y$, defined by Equation B-2 (Takcshito et al., 1984),

$$c_p = \sum_{n=0}^{3} A_n^{c_p} Y^n + t\sum_{n=0}^{3} B_n^{c_p} Y^n + t^2 \cdot \sum_{n=0}^{3} C_n^{c_p} Y^n \tag{B-2}$$

The mixed heat is written as a function of R22 molar concentration $Y$ (Takcshito et al., 1984). $A_n$, $B_n$, $C_n$, $A_n^{c_p}$, $B_n^{c_p}$, $C_n^{c_p}$ and $G_n$ are the constant coefficients

which have been shown in Table A2.

$$\Delta H_m = Y(1-Y)\cdot\sum_{n=1}^{4} G_n(1-2Y)^{n-1} \tag{B-3}$$

Molar enthalpy of solution is defined as a function of specific heat $c_p$, mixed heat $\Delta H_m$, molar concentration of R22, $Y$, molecular weights of DEGDME $M_D$ and R22 $M_{R22}$, thermal equivalent of work $J$, and solution temperature $t$. Molar enthalpy is expressed by Equation B-4 (Takcshito et al., 1984),

$$H = \frac{\Delta H_m + \int_{10}^{t} c_p dt + \int_{0}^{10} c_p(Y=0)dt + Y(\int_{0}^{10} c_p(Y=1)dt - \int_{0}^{10} c_p(Y=0)dt)}{J(M_D(1-Y)+M_{R22}Y)} + 100 \tag{B-4}$$

Based on the first law of thermodynamics, each components heat load was defined. In the generator, the thermal load consists of solution enthalpy and mass flow rate, and working medium mass flow rate and enthalpy, which can be defined by Equation B-5 (Wu et al., 2020),

$$Q_{gen} = m_{wf}\cdot h_{R1} + m_w \cdot h_{S1} - m_s \cdot h_{S6} \tag{B-5}$$

Since the combustion of natural gas is to driven the generator, the thermal load $Q_{gen}$ is defined by Equation B-6,

$$Q_{gen} = q \cdot V_{ng} \tag{B-6}$$

where $V_{ng}$ is the natural gas flow rate of the and $q$ is the calorific value.

Heat is transferred from ambient air to refrigerant in the evaporator, with heat determined by Equation B-7 (Wu et al., 2020),

$$Q_{eavp} = m_{wf}(h_{R6} - h_{R5}) \tag{B-7}$$

Refrigerant vapor condenses and releases heat to the supply to the target temperature water in the condenser. A mixed heat of solution and refrigerant heats

the supply water in the absorber. The heating capacity is consisted of absorber heat load and condenser heat load, which is shown as:

$$Q_{cond} = m_r(h_{R2} - h_{R2}) = c_{p.w}\rho_w V_w(T_{W3} - T_{W2}) \quad \text{(B-8)}$$

$$Q_{abs} = m_r \cdot h_{R7} + m_w \cdot h_{S3} - m_s \cdot h_{S4} = c_{p.w}\rho_w V_w(T_{W2} - T_{W1}) \quad \text{(B-9)}$$

$$Q_{hc} = Q_{cond} + Q_{abs} = c_{p.w}\rho_w V_w(T_{W3} - T_{W1}) \quad \text{(B-10)}$$

The heat load in the heat exchanger-II and solution heat exchanger are calculated by Equations B-11 and B-12, respectively,

$$Q_{she} = m_s(h_{S6} - h_{S5}) = m_w(h_{S1} - h_{S2}) \quad \text{(B-11)}$$

$$Q_{he-II} = m_r(h_{R4} - h_{R3}) = m_r(h_{R7} - h_{R6}) \quad \text{(B-12)}$$

The COP of the system is written by Equation B-13 (Wu et al., 2020),

$$COP = \frac{Q_{cond} + Q_{abs}}{Q_{gen}/\eta_b + W_p} \quad \text{(B-13)}$$

## References


Liu Y, Chen HY, Zhang LM, Wu XG, Wang XJ., 2020. Energy consumption prediction and diagnosis of public buildings based on support vector machine learning: A case study in China. Journal of Cleaner Production. 272, 122542. https://doi.org/10.1016/j.jclepro.2020.122542.

Zhang LH, Ma X, Wang YX, Song R, Li JJ, Yuan WC, Zhang SS., 2020. The increasing district heating energy consumption of the building sector in China: Decomposition and decoupling analysis. Journal of Cleaner Production. 271, 122696. https://doi.org/10.1016/j.jclepro.2020.122696.

Wu ZX, Zhang YF, He ZL, Yu XH, Ma XL, Sheng Y., 2019. Performance investigation of a bi-functional integration system for power and heat supply. Applied thermal engineering. 148, 714-721. https://doi.org/10.1016/j.applthermaleng.2018.11.102.

International Energy Efficiency (IEA). Energy Efficiency 2018. OECD; 2018. https://doi.org/10.1787/ 9789264024304-en.

Khalid R., 2019. Design, Economics, and Real-Time Optimization of a Solar/Natural Gas Hybrid Power Plant (Doctoral dissertation, The University of Utah).

Wei WZ, Ni L, Zhou CH, Wang W, Xu LF, Yang YH et al., 2020. Technical, economic and environmental investigation on heating performance of quasi-two stage compression air source heat pump in severe cold region. Energy and Buildings. 223,110152. https://doi.org/10.1016/j.enbuild.2020.110152.

Lu D, Chen GF, Gong MQ, Bai Y, Xu QY, Zhao YX et al., 2019. Thermodynamic and economic analysis of a gas-fired absorption heat pump for district heating with cascade recovery of flue gas waste heat. Energy Conversion and Management. 185, 87-100. https://doi.org/10.1016/j.enconman.2019.01.110.

Wu W, You T, Wang BL, Shi WX, Li XT., 2014. Simulation of a combined heating, cooling and domestic hot water system based on ground source absorption heat pump. Applied Energy. 126, 113-122. https://doi.org/10.1016/j.apenergy.2014.04.006.

Anna N, Robert S., 2014. Comparison of LCA results of low temperature heat plant using electric heat pump, absorption heat pump and gas-fired boiler. Energy

Conversion and Management. 87, 647-652. https://doi.org/10.1016/j.enconman.2014.07.032.

Zhang QL, Cao MK, Zhang QY, Di HF., 2015. Research on a New District Heating Method Combined with Hot Water Driven Ground Source Absorption Heat Pump. Energy Procedia. 75, 1242-1248. https://doi.org/10.1016/j.egypro.2015.07.172.

Garimella S, Christensen RN, Lacy D., 1996. Performance evaluation of a generator-absorber heat-exchange heat pump. Applied Thermal Engineering. 16(7), 591-604. https://doi.org/10.1016/1359-4311(95)00041-0.

Wu W, Wang BL, Shang S, Shi WX, Li XT., 2016. Experimental investigation on $NH_3$-$H_2O$ compression-assisted absorption heat pump (CAHP) for low temperature heating in colder conditions. International Journal of Refrigerant. 67, 109-24. https://doi.org/10.1016/j.ijrefrig.2016.03.019.

Wu W, Wang BL, You T, Wang J, Shi WX, Li XT., 2018. Compression-assisted absorption cycles using ammonia and various ionic liquids for cleaner heating. Journal of Cleaner Production. 195, 890-907. https://doi.org/10.1016/j.jclepro.2018.05.270.

Wu W, Zhang HY, You T, Li XT., 2017. Performance comparison of absorption heating cycles using various low-GWP and natural refrigerants. International Journal of Refrigerant. 82, 56-70. https://doi.org/10.1016/j.ijrefrig.2017.07.004.

Lu D, Bai Y, Zhao YX, Dong XQ, Gong MQ, Luo RC et al., 2020. Experimental investigations of an absorption heat pump prototype with intermediate process

for residential district heating. Energy Conversion and Management. 204, 112323. https://doi.org/10.1016/j.enconman.2019.112323.

Shang S, Li XT, Chen W, Wang BL, Shi WX., 2017. A total heat recovery system between the flue gas and oxidizing air of a gas-fired boiler using a non-contact total heat exchanger. Applied Energy. 207, 613-23. https://doi.org/10.1016/j. apenergy.2017.05.169.

Khalid R, Seyed M S, Kody M.Powell., 2019. Dynamic simulation, control, and performance evaluation of a synergistic solar and natural gas hybrid power plant. Energy Conversion and Management. 179, 270-285. https://doi.org/10.1016/j.enconman.2018.10.054

Yang B, Jiang Y, Fu L, Zhang SG., 2018. Experimental and theoretical investigation of a novel full-open absorption heat pump applied to district heating by recovering waste heat of flue gas. Energy and Building. 173, 45-5. https://doi.org/10.1016/j.enbuild.2018.05.021.

Qu M, Omar A, Yin HX., 2014. New configurations of a heat recovery absorption heat pump integrated with a natural gas boiler for boiler efficiency improvement. Energy Conversion and Management. 87, 175-184. https://doi.org/10.1016/j. enconman.2014.06.083.

Hu B, Yan HZ, Wang RZ., 2019. Modeling and simulation of a falling film evaporator for a water vapor heat pump system. Applied Energy. 255, 113851. https://doi.org/10.1016/j.apenergy.2019.113851.

Robabeh. A.H, Scott J.O., 2020. An elliptic numerical analysis of water vapour

absorption into a falling film in vertical parallel plate channels. International Journal of Heat and Mass Transfer. 150, 119266. https://doi.org/10.1016/j.ijheatmasstransfer.2019.119266.

Saeed A, Ali J. Heat transfer evaluation and economic characteristics of falling film brine concentrator in zero liquid discharge processes. Journal of Cleaner Production. 2021, 124892. https://doi.org/10.1016/j.jclepro.2020.124892.

Liu F, Sui J, Liu H, Jin HG., 2017. Experimental studies on a direct-steam-generation absorption heat transformer built with vertical falling-film heat exchangers. Experimental Thermal and Fluid Science. 83, 9-18. https://doi.org/10.1016/j.expthermflusci.2016.11.033.

Cheng H, Ju YL, Fu YZ., 2020. Experimental study on heat transfer characteristics of cooling falling film outside a vertical tube in open rack vaporizer. Applied Thermal Engineering. 172, 115187. https://doi.org/10.1016/j.applthermaleng.2020.115187.

Liu SL, Mu XS, Shen SQ, Li C, Wang BY., 2021. Experimental study on the distribution of local heat transfer coefficient of falling film heat transfer outside horizontal tube. International Journal of Heat and Mass Transfer. 170, 121031. https://doi.org/10.1016/j.ijheatmasstransfer.2021.121031

Nico M, Fabian S, Bernd B, Klaus S., 2020. Design and analysis of an ammonia-water absorption heat pump. Applied Thermal Engineering. 165, 114531. https://doi.org/10.1016/j.applthermaleng.2019.114531.

Yuan H, Zhang J, Huang XK, Mei N., 2018. Experimental investigation on binary

ammonia-water and ternary ammonia-water-lithium bromide mixture-based absorption refrigeration systems for fishing ships. Energy Conversion and Management. 166, 13-22. https://doi.org/10.1016/j.enconman.2018.04.013.

Wu ZX, You SJ, Zhang H, Wang YR, Wei S, Jiang Y et al., 2020. Performance analysis and optimization for a novel air-source absorption heat pump. Energy Conversion and Management. 233, 113423. https://doi.org/10.1016/j.enconman. 2020.113423

Ando E, Takcshito I., 1984. Residential gas-fired absorption heat pump based on R22-DEGDME Pair, Part 1: thermodynamic properties of R22-DEGDME Pair. International Journal of Refrigeration. 7, 181-185. https://doi.org/10.1016/0140 -7007(84)90098-7.

Robabeh A.H, Scott J. O., 2018. Fully coupled two-phase numerical model for falling film absorption in a vertical parallel plate channel. International Journal of Refrigerant. 95, 108-121. https://doi.org/10.1016/j.ijrefrig.2018.08.009.

M. Mittermaier, F. Ziegler., 2015. Theoretical evaluation of absorption and desorption processes under typical conditions for chillers and heat transformers. International Journal of Refrigeration. 59, 91-101. https://doi.org/10.1016/j.ijrefr ig.2015.07.015.

M. Mittermaier, P. Schulze, F. Ziegler., 2014. A numerical model for combined heat and mass transfer in a laminar liquid falling film with simplified hydrodynamics. International Journal of Heat and Mass Transfer. 70, 990-1002. https://doi.org/10.1016/j.ijheatmasstransfer.2013.11.075.

E.García- J.Castro, J.Farnós, C.Oliet., 2019. Numerical and experimental study of absorption of $H_2O$ vapor in wavy falling film of LiBr aqueous solution in vertical tubes and in presence of non-absorbables. International Journal of Refrigeration. 100, 184-195. https://doi.org/10.1016/j.ijrefrig.2019.01.022.

Wu ZX, Sha L, Zhao MZ, Wang XY, Ma HT, Zhang YF., 2020. Performance analyzes and optimization of a reverse Carnot cycle-organic Rankine cycle dual-function system. Energy Conversion and Management. 212, 112787. https://doi.org/10.1016/j.enconman.2020.112787.

Jain V, Sachdeva G., 2017. Energy, exergy, economic (3E) analyzes and multi-objective optimization of vapor absorption heat transformer using NSGA-II technique. Energy Conversion and Management. 148, 1096-1113. https://doi.org/10.1016/j.enconman.2017.06.055.

Wang YZ, Zhao J, Wang Y, An Q.S., 2017. Multi-objective optimization and grey relational analysis on configurations of organic Rankine cycle. Applied Thermal Engineering. 114, 1355-1363. https://doi.org/10.1016/j.applthermaleng.2016.10.075.

Wu ZX, Zhang YF, Sheng Y., 2019. Energy, exergy, economic(3E) analysis and multi-objective optimization of a novel dual functional integration system. Energy Conversion and Management. 199, 111962. https://doi.org/10.1016/j.enconman.2019.111962.

Wu ZX, Sha L, Yang XC, Zhang YF., 2020. Performance evaluation and working fluid selection of combined heat pump and power generation system (HP-PGs)

using multi-objective optimization. Energy Conversion and Management. 221, 113164. https://doi.org/10.1016/j.enconman.2020.113164.

Takcshito I, Yamamoto Y, Harada T, Wakamatsu N., 1984. Residential gas-fired absorption heat pump based on R22-DEGDME Pair, Part 2: design, computer simulation and testing of a prototype. International Journal of Refrigeration. 7, 313-321. https://doi.org/10.1016/0140-7007(84)90121-X.